

Venus' upper atmosphere revealed by a GCM: I. Structure and variability of the circulation

Thomas Navarro, Gabriella Gilli, Gerald Schubert, Sébastien Lebonnois, Franck Lefèvre, Diogo Quirino

▶ **To cite this version:**

Thomas Navarro, Gabriella Gilli, Gerald Schubert, Sébastien Lebonnois, Franck Lefèvre, et al.. Venus' upper atmosphere revealed by a GCM: I. Structure and variability of the circulation. Icarus, 2021, 366 (September), pp.114400. 10.1016/j.icarus.2021.114400 . insu-03162299v2

HAL Id: insu-03162299

https://insu.hal.science/insu-03162299v2

Submitted on 16 Jun 2021

HAL is a multi-disciplinary open access archive for the deposit and dissemination of scientific research documents, whether they are published or not. The documents may come from teaching and research institutions in France or abroad, or from public or private research centers.

L'archive ouverte pluridisciplinaire **HAL**, est destinée au dépôt et à la diffusion de documents scientifiques de niveau recherche, publiés ou non, émanant des établissements d'enseignement et de recherche français ou étrangers, des laboratoires publics ou privés.



Distributed under a Creative Commons Attribution - NoDerivatives 4.0 International License

Icarus 366 (2021) 114400

Contents lists available at ScienceDirect

Icarus

journal homepage: www.elsevier.com/locate/icarus

Research Paper

Venus' upper atmosphere revealed by a GCM: I. Structure and variability of the circulation

Thomas Navarro [a,b,*], Gabriella Gilli [c,d], Gerald Schubert [a], Sébastien Lebonnois [e], Franck Lefèvre [f], Diogo Quirino [c,d]

[a] Department of Earth, Planetary and Space Sciences, University of California, Los Angeles, CA, USA
[b] McGill Space Institute, McGill University, Montreal, Canada
[c] Instituto de Astrofisica e Ciências do Espaço (IA), OAL, Tapada da Ajuda, PT1349-018 Lisboa, Portugal
[d] Faculdade de Ciências, Campo Grande, PT1749-016 Lisboa, Portugal
[e] Laboratoire de Météorologie Dynamique (LMD) Paris, France
[f] IPSL/LATMOS, Paris, France

ARTICLE INFO

Keywords:
Venus
GCM
Upper atmosphere
Atmospheric circulation
Airglow
Kelvin wave
Singlet oxygen

ABSTRACT

A numerical simulation of the upper atmosphere of Venus is carried out with an improved version of the Institut Pierre-Simon Laplace (IPSL) full-physics Venus General Circulation Model (GCM). This simulation reveals the organization of the atmospheric circulation at an altitude above 80 km in unprecedented detail. Converging flow towards the antisolar point results in supersonic wind speeds and generates a shock-like feature past the terminator at altitudes above 110 km. This shock-like feature greatly decreases nightside thermospheric wind speeds, favoring atmospheric variability on a hourly timescale in the nightside of the thermosphere. A ~5-day period Kelvin wave originating in the cloud deck is found to substantially impact the Venusian upper atmosphere circulation. As the Kelvin wave impacts the nightside, the poleward meridional circulation is enhanced. Consequently, recombined molecular oxygen is periodically ejected to high latitudes, explaining the characteristics of the various observations of oxygen nightglow at 1.27 μm. An analysis of the simulated 1.27 μm oxygen nightglow shows that it is not necessarily a good tracer of the upper atmospheric dynamics, since contributions from chemical processes and vertical transport often prevail over horizontal transport. Moreover, dayside atomic oxygen abundances also vary periodically as the Kelvin wave momentarily decreases horizontal wind speeds and enhances atomic oxygen abundances, explaining the observations of EUV oxygen dayglow. Despite the nitrogen chemistry not being currently included in the IPSL Venus GCM, the apparent maximum NO nightglow shifted towards the morning terminator might be explained by the simulated structure of winds.

1. Introduction

The circulation of the Venusian atmosphere is dominated by the westward retrograde zonal superrotation (RZS) of the cloud deck at altitudes up to 70 km. Higher up in the thermosphere, the strong day-to-night thermal gradient induces a Subsolar to Antisolar (SS–AS) circulation, with air flowing from the dayside to the nightside (Bougher et al., 1997; Schubert et al., 2007). Between approximately 90 and 120 km of altitude, the circulation changes from RZS to SS–AS, forming a transition region between the two circulations.

Understanding in detail the mechanisms at stake in the upper atmosphere is crucial for many key questions arising for Venus, and for slowly rotating, highly irradiated exoplanets in general. The cause and maintenance of the RZS remains one the largest Venusian mysteries. The transition region is where the RZS ends and may shed light on such a mystery by assessing the angular momentum exchanges between the upper and lower atmospheres. The upper atmosphere is critical for atmospheric escape, as it is the location where light elements are formed, transported, and interact with the solar wind. It is also a crucial region for the stability of carbon dioxide as the main constituent of the Venusian atmosphere. Carbon dioxide is photochemically dissociated and recombined in the upper atmosphere, but there is no consensus on why it is orders of magnitude more abundant than e.g. carbon monoxide or dioxygen, despite being recycled continuously (Marcq et al., 2018). Airglow emissions that are present in the transition region due to excited chemical species from recombination (such as O_2 and NO) in the transition region have been proposed as a possible medium

* Corresponding author at: Department of Earth, Planetary and Space Sciences, University of California, Los Angeles, CA, USA.
E-mail address: tnavarro@epss.ucla.edu (T. Navarro).

https://doi.org/10.1016/j.icarus.2021.114400
Received 18 September 2020; Received in revised form 19 February 2021; Accepted 22 February 2021
Available online 6 March 2021
0019-1035/© 2021 The Authors. Published by Elsevier Inc. This is an open access article under the CC BY-NC-ND license (http://creativecommons.org/licenses/by-nc-nd/4.0/).

for detecting seismic waves from remote observations and assess if Venus is geologically active in the present day (Didion et al., 2018).

Many unresolved questions pertaining to the observations of Venus' upper atmospheric circulation still prevail after the space mission Venus Express (VEx) era (Drossart et al., 2007; Svedhem et al., 2007; Gérard et al., 2017). Among them is the cause of the variability and spatial patterns of horizontal wind speeds and O_2 and NO nightglows. In order to close the large-scale circulation between the RZS and the SS–AS circulations, an upward flow must exist on the dayside and a downward flow on the nightside. The downward vertical motion on the nightside is the location of the recombination of chemical species that create a variety of nightglows (O_2, NO, OH). For instance, singlet oxygen O_2 ($^1\Delta_g$), the end product of the recombination of atomic oxygen, creates a nightglow at 1.27 μm and observed statistically to be evenly distributed around the Anti-Solar (AS) point (Soret et al., 2012). Such an observation suggests that the AS point is, on the average, where the SS–AS converges. However, rapid changes on a daily timescale of individual patches or large scale elongated structures of O_2 nightglow at low and high latitudes (Crisp et al., 1996; Lellouch et al., 1997; Hueso et al., 2008; Gérard et al., 2014; Soret et al., 2014) do not match with the simple view of a steady, fixed downward flux centered at the AS point. Moreover, NO nightglow is produced by the reaction between atomic nitrogen and oxygen, at an altitude of 115 km, and located on average towards the morning terminator (Stewart et al., 1980; Stiepen et al., 2013). The interpretation of this observation is challenging, since the O_2 nightglow happens at an altitude of 95 km, thus suggesting an unknown mechanism produces a westward shift towards the morning terminator at 115 km, but not at 95 km. Another class of airglow is the Extreme Ultra-Violet (EUV) dayglow due to photon emission at 135 nm by excited atomic oxygen on the dayside upper atmosphere, above 130 km. Periodic variations of this dayglow, notably 3-day and 4-day ones, have been observed by the Hisaki space telescope (Masunaga et al., 2015), mostly on the morning side (Masunaga et al., 2017). Simultaneous observations with winds retrieved from tracking cloud-top features by the Akatsuki orbiter (Nakamura et al., 2016) and Hisaki suggest a coupling between the RZS and the SS–AS circulations by thermospheric gravity waves excited by a cloud-level Kelvin wave (Nara et al., 2020).

Another kind of unexplained observation is the atmospheric variability of the upper atmosphere observed from both the ground and the Venusian orbit. Clancy et al. (2008) observed daily fluctuations of CO volume mixing ratio of 30%–50% and temperature of 5–20 K on the evening terminator above 95 km from Doppler shift of sub-mm and mm CO lines. Clancy et al. (2012) observed a sizeable nighttime variability of 50%–70% of horizontal wind speeds at an altitude of 110 km from hourly to interannual timescales, with a complex superimposition of SS–AS and RZS winds, as confirmed by Clancy et al. (2015). Sornig et al. (2008), Sornig et al. (2012) also observed a large variability of wind speeds at 110 km on the dayside, from heterodyne non-LTE (Local Thermal Equilibrium) infrared CO_2 emission at 10 μm, and did not detect superrotation at the equator at 110 km, but at a latitude of 33°. Sornig et al. (2013) then detected wind variability and interpreted the location of the converging point of the SS–AS circulation to vary from the west or east of the midnight meridian in less than a month. Temperature measurements by VEX also showed a spatial variability of the nightside temperature (Piccialli et al., 2015). Krause et al. (2018) measured terminator temperature at 110 km with a ground-based spectrometer, showing that temperature variability is the same order on long (6 years) and on short timescales (< 10 days).

Numerical models are tools of choice for interpreting observations and exploring the mechanisms at stake in the upper atmosphere circulations, where direct wind measurements are usually very scarce. As a matter of fact, the SS–AS circulation was first hypothesized from a two-dimensional numerical model (altitude vs. solar zenith angle) (Dickinson and Ridley, 1972). Later on, three-dimensional General Circulation Models (GCM) revealed the details of the circulation of the upper atmosphere. Such models reproduce the SS–AS circulation (Bougher et al., 1988a), and include a photochemical package (Brecht et al., 2011; Brecht and Bougher, 2012; Gilli et al., 2017), a parameterization of unresolved gravity waves (Zhang et al., 1996; Zalucha et al., 2013; Hoshino et al., 2013; Gilli et al., 2017). The inclusion of planetary-scale waves generated in the lower atmosphere shows that a Kelvin wave can impact the upper atmosphere dynamics and the O_2 nightglow (Hoshino et al., 2012; Nakagawa et al., 2013; Brecht et al., 2021).

In this article, we build on the work by Gilli et al. (2017) and investigate in detail the nightside circulation from the cloud top, and up to 150 km, with the IPSL Venus GCM, while a companion article (Gilli et al., 2021) addresses a fine-tuning in the non-LTE parameterization, which improves the representation of thermal structure above 90 km, and provides data-model validation with a comprehensive selection of temperature and density measurements from VEx and ground-based telescopes. Specifics of the simulation done for this work are described in Section 2. Section 3 details the structure of the nightside circulation, and Section 4 addresses its variability. Section 5 shows the impact of the Kelvin wave on the whole upper atmosphere. Section 6 presents the impact of the circulation on the O_2 and EUV oxygen airglows, then Section 7 discusses the use of O_2 nightglow as a tracer of dynamics. Finally, Section 8 discusses the findings and limitations of such a simulation, and a conclusion is given in Section 9.

2. GCM simulation

The GCM used for this study is the Institut Pierre-Simon Laplace (IPSL) Venus GCM, a full-physics, ground-to-thermosphere model (Lebonnois et al., 2010; Gilli et al., 2017) able to simulate the RZS circulation reasonably well to observed values (Lebonnois et al., 2016; Garate-Lopez and Lebonnois, 2018). It notably includes a radiative transfer with solar heating rates (Crisp, 1986) and infrared net exchanges rates (Eymet et al., 2009), Magellan topography, a Mellor–Yamada level 2.5 scheme for the boundary layer (Mellor and Yamada, 1982), a temperature-dependent heat capacity to reflect deviation of the deep atmosphere from the assumption of an ideal gas. This model has been extended to the thermosphere (Gilli et al., 2017), up to 3×10^{-6} Pa (approximately 150 km), with the inclusion of non-LTE processes, near-IR heating, CO_2 thermal cooling at 15 μm, molecular diffusion, and thermal conduction. It also includes a cloud and photochemical model for 34 chemical species relevant to the carbon, oxygen, chlorine, and sulfur chemistry, and are dynamically transported by the GCM (Stolzenbach, 2016).

The present setup with the inclusion of the upper atmosphere has been improved since its first development presented in Gilli et al. (2017). First, the non-LTE parameterization, detailed in the companion paper Gilli et al. (2021), was fine-tuned to temperature observations of VEx, resulting in reduced (factor 2) heating/cooling peaks at 0.5 Pa (about 100 km) at daytime and reduced heating rates (factor 3) at morning/evening terminators around 0.1 Pa, compared to Gilli et al. (2017). At nightime, radiative tendencies are affected by changes in the non-LTE parameterization mostly in the thermosphere, above 110 km approximately, suggesting that the region below is dominated by dynamical tendencies. Second, the present simulation now employs the same heating rates as in Garate-Lopez and Lebonnois (2018), with a latitude-dependent cloud top altitude (Haus et al., 2015) and the radiative effects of a sub-cloud haze, which resulted in increased zonal wind values from 15 to 45 m s^{-1} below the cloud deck at 45 km, in better agreement with values of 60 m s^{-1} measured in-situ by Pioneer Venus (Schubert, 1983). Third, we increased the horizontal resolution of the Laboratoire de Météorologie Dynamique Zoom (LMDZ) longitude–latitude grid dynamical core (Hourdin et al., 2006) from the one employed by Gilli et al. (2017), from 7.5° × 5.625° (48 × 32 grid points) to 3.75° × 1.875° (96 × 96). While this increased resolution is not a novelty for the lower atmosphere of Venus with the IPSL Venus GCM (Lebonnois et al., 2016; Garate-Lopez and Lebonnois, 2018;

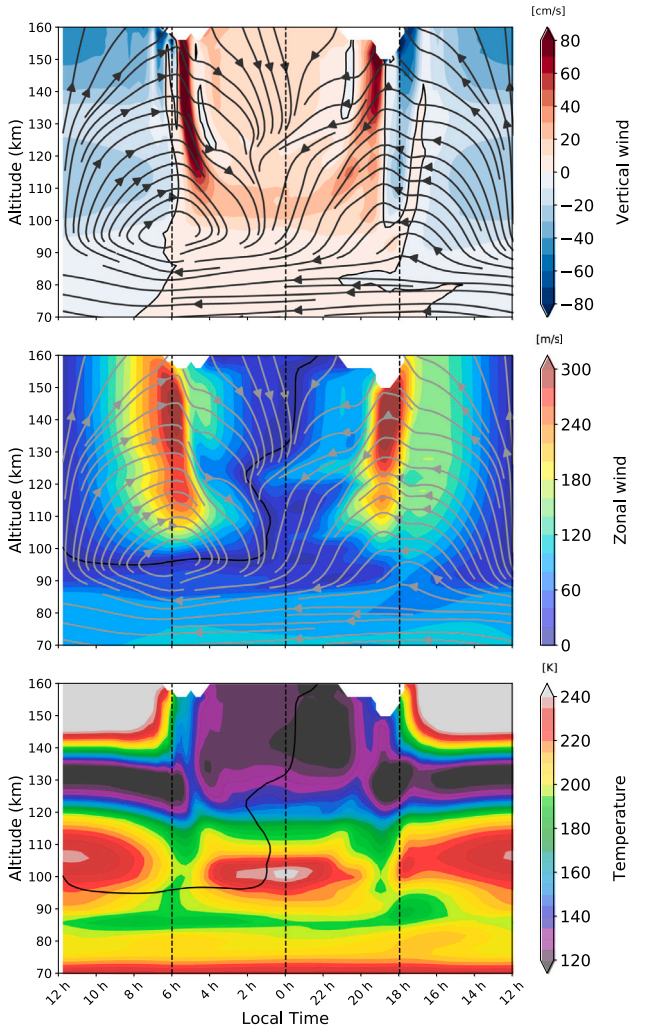


Fig. 1. (top) Vertical, (middle) absolute zonal wind speeds, and (bottom) temperature at the equator averaged for one Vd. Streamlines show the circulation in the altitude vs. local time plan constructed from the average wind field shown in the top and middle panels. Thick solid line indicates where zonal wind values are zero.

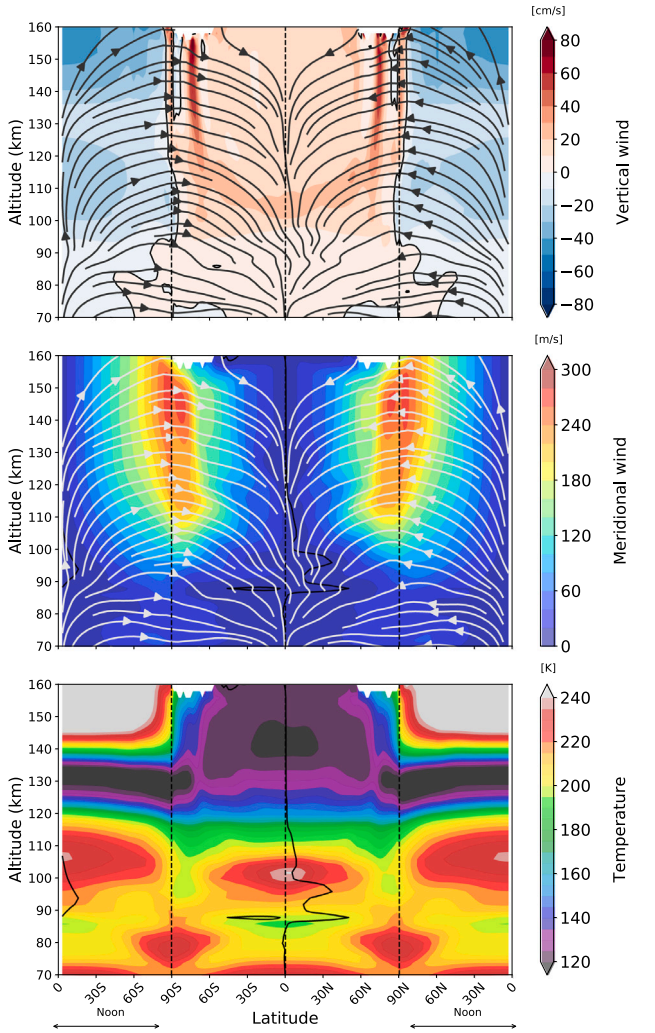


Fig. 2. Same as Fig. 1, but for absolute meridional wind speeds along the noon-midnight meridians averaged for one Vd.

Navarro et al., 2018) or other GCMs at a higher (Ando et al., 2016; Takagi et al., 2018) or much higher (Kashimura et al., 2019) resolution, it is the highest resolution ever used for the upper atmosphere of Venus, compared for instance to 5° × 5° in Brecht and Bougher (2012), Brecht et al. (2021), or T21 (11.25° × 2.8125°) in Hoshino et al. (2012, 2013) and Nakagawa et al. (2013). Sugimoto et al. (2014) studied waves with the AFES GCM at a T63 (192 × 96) resolution and a model top at 120 km. However, their setup did not include any parameterization of upper atmospheric processes and they implemented a sponge layer starting at 80 km, thus efficiently damping atmospheric circulation in the upper atmosphere. Brecht and Bougher (2012) deemed necessary an increased resolution in order to resolve the sharp horizontal temperature gradients near the terminators, and indeed resulted in substantial changes in our simulations, as will be detailed below. The major hurdle in implementing such an increased resolution is the high numerical instability of the simulations, with instabilities leading to unrealistic temperatures within a few tens of hours near the AS point in the upper atmosphere. To overcome this issue, we first ran the IPSL Venus GCM during one solar Venus day (Vd) from a converged initial state of the lower atmosphere obtained after 300 Vd in Garate-Lopez and Lebonnois (2018), and simplified prescribed altitude and solar zenith angle dependent distributions for CO_2, CO, O, and N_2 species above 90 km (Hedin et al., 1983). We thus obtained an initial state stable for the full interactive photochemical package, suggesting that the numerical instabilities may arise from feedback loops between the upper atmosphere heating rates, dynamic chemical species, and the non-converged circulation of the downward moving flow near the AS point. We then obtained, after 29 Vd, a converged simulation with constant 1 Vd-averaged SS–AS wind speeds, without prescribed chemical species.

Additionally, the IPSL Venus GCM uses a stochastic parameterization of non-orographic gravity waves (Lott et al., 2012). Gravity waves are assumed to be generated at the top of the convective cells, located at about 55 km on Venus, propagate upwards, and break in the upper atmosphere. These waves were found to impact the circulation of the upper atmosphere (Zalucha et al., 2013; Gilli et al., 2017). To correctly implement this parameterization with the increased resolution, we corrected the minimal horizontal wavenumber k_{min} of individual waves:

$$k^*_{min} = max(k_{min}, \frac{\pi}{A}) \quad (1)$$

with A the surface area of the grid cell.

3. Average structure of the nightside circulation

3.1. Horizontal wind

Atmospheric fields above 70 km and averaged for 1 Vd are shown as a function of local time in Fig. 1, of latitude in Fig. 2, and as maps

at different altitudes in Fig. 3. The circulation is dominated by the SS–AS circulation above 100 km of altitude, with winds converging from the SS point to the AS point, and wind speed exceeding 300 m s^{-1} at the terminator. The RZS circulation is dominant below 85 km (Fig. 1), with values around 100 m s^{-1} at the cloud top (~ 70 km). Between 90 and 105 km approximately lies a transition region consisting of a reversal of the zonal wind from retrograde (westwards) to prograde (eastwards) values between local times 0 h and 12 h (Fig. 1). Figs. 1 and 3 also show an asymmetry of the SS–AS zonal flow between the morning and evening branches and between 120 and 130 km due to the breaking of non-orographic gravity waves at those altitudes (see companion paper). The wind is slightly more westwards on the average, with convergence shifted away between midnight and 2 h between about 100 and 130 km, as apparent in the zero zonal wind contour of Fig. 1. Conversely, the SS–AS meridional flow is symmetric between the Northern and Southern hemispheres (Fig. 2), as the non-orographic gravity waves' drag is weaker on the meridional direction compared to the zonal one. Because of this structure, a point with null wind speed (both zonal and vertical) exists at the equator at local time 6 h, and between altitudes 95 to 100 km (see average equatorial wind streamlines in Fig. 1).

3.2. Temperature

Temperature decreases with altitude until the transition region, where local maxima of 240 K are centered near the Sub-Solar (SS) and AS point (bottom panels of Figs. 1 and 2). The warming at the SS point between altitudes 100 and 110 km is due to near-IR heating produced by CO_2 molecules non-LTE absorption of solar radiation, as pointed out by Gilli et al. (2017) and Brecht and Bougher (2012) and observed by the VIRTIS instrument on board VEx (Gilli et al., 2015). The warming near the AS point has also been observed with VEx (Bertaux et al., 2007; Piccialli et al., 2015) and is due to the downward flow of day-to-night air by adiabatic compression and advection from the dayside, as shown by Gilli et al. (2017) and Brecht and Bougher (2012). Above these warm layers, temperature decreases anew with altitude, until EUV heating warms the dayside above 140 km. The cold nightside temperatures above 120 km and below 140 km observed by Pioneer Venus (Schubert et al., 1980) are due to CO_2 cooling at 15 μm (Gilli et al., 2017). The terminators are cooler than other local times at altitudes 95 to 115 km as shown in Figs. 1, 2, and 3. This result is not in agreement with Piccialli et al. (2017), probably because they used a-priori CO profiles from Clancy et al. (2012) up to 100 km, and a constant value above, whereas our model predicts instead CO volume mixing ratio decreasing above that altitude (see companion paper Gilli et al., 2021). A more detailed comparison of the temperature structure of this simulation is given in Gilli et al. (2021).

3.3. Shock-like feature and downward motion near the terminator

These results are in general agreement with previously published GCM studies and observations, and the mechanisms at stake understood to a large extent. However, our simulations reveal a particular structure consisting of downward vertical speeds maximal near the terminator on the nightside, with larger values near the morning terminator than the evening terminator, reaching 100 cm s^{-1} above 120 km (see top panel in Fig. 1). This downward motion is associated with sharp horizontal gradients of horizontal winds (Figs. 1, 2, and 3), with a decrease reaching up to 200 m s^{-1} over a distance of 500 km and less. A local increase of temperature of up to 40 K is also associated with this downward motion (Figs. 1, 2, 3 and 4), producing a nightside "hot ring" feature above 120 km, well visible in the time-averaged field at 130 km in Fig. 3, or in the instantaneous field at 120 km in Fig. 8.

The nature of this structure is not straightforward. It is reminiscent of the "tongue" of downward vertical motion and local heating simulated by Dickinson and Ridley (1975, 1977) with a 2D altitude-solar zenith angle model, or Bougher et al. (1986) with a 3D GCM. The tongue-like shape is apparent in the vertical, horizontal winds and temperature fields in Figs. 1 and 2, with the structure moving away from the terminator towards the AS point as it gets lower in altitude. According to Dickinson and Ridley (1975), the cause of the hot ring is adiabatic heating from the downward motion caused by the decrease in altitude of isobars past the terminator.

However, there is a major difference between our simulation and these past works. In our simulation, the horizontal wind speed is higher, with values greater than 300 m s^{-1} at an altitude of 130 km, compared to 250 m s^{-1} in Dickinson and Ridley (1975, 1977), and 200 m s^{-1} in Bougher et al. (1986). Our result is in agreement with more recent ground-based measurements of Doppler winds as high as 348 m s^{-1} on the morning terminator (Clancy et al., 2015). Therefore, the simulated winds are supersonic, with Mach numbers attaining a value of 2 at 130 km (Fig. 3), with the Mach number defined as $M = v/c_s$ with v the wind speed, the speed of sound $c_s = \sqrt{\gamma RT/\mathcal{M}}$, γ the heat capacity ratio, T the temperature, R the ideal gas constant, and $\mathcal{M}$ the molar mass. Given the Mach number is well above unity in our simulation, followed by a sharp wind decrease and temperature increase at altitudes above 120 km (Fig. 4), it is reasonable to investigate the presence of a supersonic shock wave as a possible cause of the structure in the vicinity of the terminator. Atmospheric supersonic shocks have been studied in the context of hot, highly irradiated, giant exoplanets (e.g. Rauscher and Menou, 2010; Heng, 2012), but quite rarely for the Venusian upper atmosphere. By considering the air densities measured by Pioneer Venus, Seiff (1982) briefly discussed the possibility of a shock in the Venusian upper atmosphere as a dissipation mechanism to slow down the SS–AS flow. Moreover, Clancy et al. (2015) estimated a Mach number 1.5 from their observations, and Hoshino et al. (2012) simulated supersonic winds, but neither mentioned a shock.

The primitive equations of the IPSL dynamical core are based on the hydrostatic equilibrium. Therefore, vertically propagating sound waves are filtered out, leaving horizontally propagating sound waves, also known as Lamb waves (Vallis, 2006, Chapter 2). Although the IPSL dynamical core can simulate Lamb waves because it is a compressible core, a standing Lamb wave steepening into a shock may not be properly simulated because of the large grid resolution (> 100 km) compared to the rapid changes of atmospheric variables over a small distance, typical of a shock.

The limitation of this GCM configuration does not preclude investigating the possibility of a shock in the Venusian upper atmosphere. With a hydrostatic dynamical core having the same limitations, Showman et al. (2009) reported a structure of strong convergence and temperature increase on a narrow region for a hot Jupiter at 1 mbar, while Rauscher and Menou (2010) discussed the nature of a similar feature and concluded it may be a Lamb wave. Drawing on this result, Fromang et al. (2016) performed simulations using a dynamical core with a proper treatment for shocks, eventually showing that hot Jupiter were prone to shocks. This useful result is pertinent for our case, as it proves that features such as Lamb waves with a limited dynamical core can be the first clue that shocks may be simulated, and actually exist, in the Venusian upper atmosphere. Future dedicated studies may be tackled with a more suitable numerical code, for instance a finite-volume one, with a higher resolution near the terminator.

One way to detect shock-like features in a numerical code is to consider the variable $\eta = -\frac{\Delta x \nabla \cdot \mathbf{v}}{c_s}$, with Δx the horizontal grid spacing. Zhu et al. (2013) and Fromang et al. (2016) empirically identified shocks wherever η has values greater than 0.2. In our simulation, we find η to be smaller than 0.2 in the upper atmosphere, except at the hot ring location, with values of η between 0.5 and 1. This fact alone strongly suggests a shock-like mechanism.

Another indication of a possible shock-like feature is the dependence of the SS–AS flow results on the horizontal resolution. Fig. 4 provides

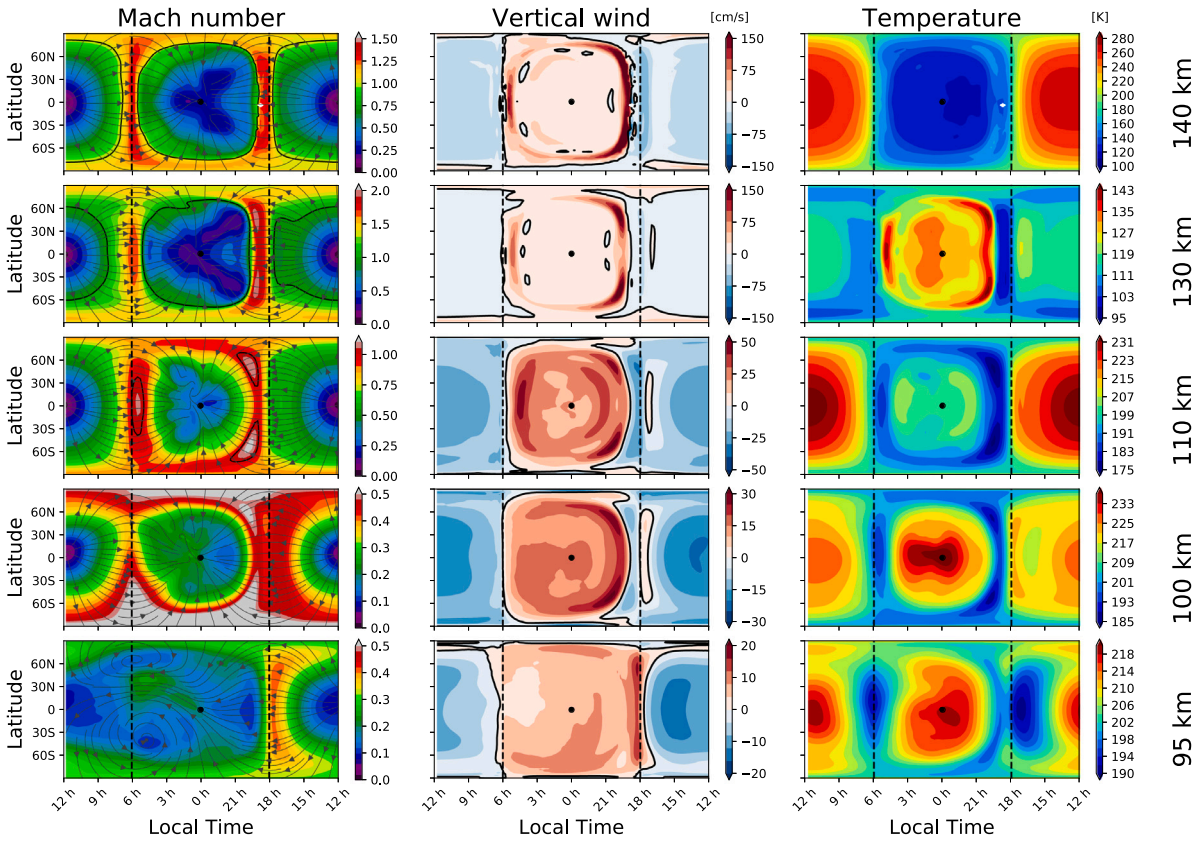


Fig. 3. Maps of Mach number, winds and temperature averaged for one Vd at 5 different altitudes. Black contour can indicate Mach number unity (left column) and zero vertical wind speed (middle column). Positive values of vertical speeds indicate downward winds.

an example of equatorial Mach number and temperature at 130 km for two resolutions: high (the present study) and low (the same employed in Gilli et al., 2017). While horizontal supersonic speeds (M >1) are obtained for both resolutions, the decrease of M below unity happens rather abruptly for the high resolution, over just two grid points past the morning and evening terminators. In contrast, the transition from supersonic to subsonic flow occurs smoothly over thousands of kilometers with the low resolution. Moreover, temperature increases just after the decrease of M for the high resolution, forming the "hot ring" feature described above, whereas no such local maximum of temperature happens for the low resolution simulation. This behavior of Mach number and temperature is in line with a shock-like feature: a decrease of M past the feature, and an increase of temperature. Shocks, including Lamb waves, happen when regions of lower density (e.g. generated by a wave) acoustically propagate faster than regions of higher density, possibly converging together if the flow is supersonic, and forming a shock. The formation and location of the shock thus depends on the profile of density perturbations and the flow's speed, temperature, and pressure along a streamline. Therefore, it makes sense that an increase in resolution is more suited to resolve the convergence of density perturbations and that a shock is eventually simulated as the resolution increases, as noted by Fromang et al. (2016) in the context of hot Jupiters.

In order to test the hypothesis of a shock-like feature against simulated values of temperatures and Mach number, we use the classic relation between temperature and Mach number of normal shock equations from one-dimensional gas dynamics theory (e.g. Liepmann and Roshko, 2001):

$$\frac{T_2}{T_1} = \frac{\left(2\gamma M_1^2 - (\gamma - 1)\right)\left((\gamma - 1)M_1^2 + 2\right)}{(\gamma + 1)^2 M_1^2} \tag{2}$$

with subscripts 1 and 2 denoting the quantities upstream and downstream of the shock-like feature, respectively. In this case, the increase of temperature is a non-isentropic, irreversible, process caused by a decrease of wind speed. Alternatively, if the temperature increase were caused by adiabatic heating of descending air as found by Dickinson and Ridley (1975, 1977), the temperature ratio would be given by the isentropic relation:

$$\frac{T_2}{T_1} = \left(\frac{P_2}{P_1}\right)^{\frac{\gamma - 1}{\gamma}} \tag{3}$$

with P the pressure. Fig. 5 compares the temperature ratio of the hot ring to Eqs. (2) and (3). At altitudes of 120 and 130 km, the general trend of the temperature increase in the hot ring is in broad agreement with a shock-like feature as given by Eq. (2). At an altitude of 140 km, the temperature increase is, in general, systematically smaller by 20% than the one expected for a shock. Isentropic compression alone does not seem to account for the simulated increase in temperature, especially at a high pressure ratio. The standard deviation between expected and simulated temperatures is smaller at 120 and 130 km for the case of a normal shock than for an isentropic compression (Fig. 5).

All in all, these results suggest that a strong (i.e. with $M > 1$ upstream and $M < 1$ downstream), normal, shock-like feature in the form a of standing Lamb wave, is present in our simulations above 120 km and is the main reason for the hot ring and strong wind deceleration. The enhanced downward motion must also play a role and will inevitably warm the descending air by adiabatic compression, but it is not the chief reason for the hot ring and wind deceleration above 120 km. Between 110 km and 120 km, where wind speeds are subsonic, adiabatic warming would then be the main reason for the persisting hot ring at those lower altitudes. Other processes also play a role, such as near-IR heating that may be responsible for slightly higher than expected temperature ratios at 120 km, and thermal conduction, possibly responsible for the lower than expected ones at 140 km. Moreover, and as pointed out by Seiff (1982), the air needs to be

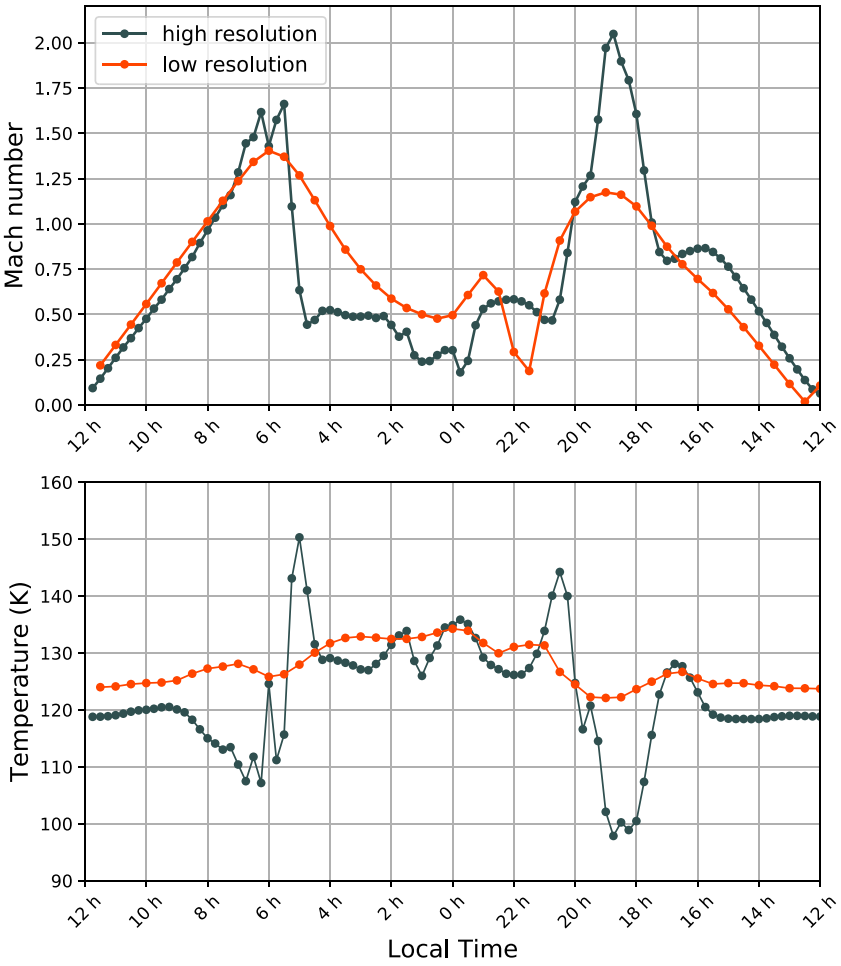


Fig. 4. Equatorial Mach number and temperature at an altitude of 130 km for high (96 × 96) and low (48 × 32) resolutions. The atmospheric flow is directed towards the AS point at local time 0 h. Dots indicate the horizontal spacing for each model resolution.

diabatically cooled to avoid high unrealistic nightside temperatures regardless of the cause of the hot ring.

It results that there is a normal shock-like feature, dissipating kinetic energy, resulting in downstream increased temperature, pressure, and density. The shock-like feature is the strongest at an altitude of 130 km, with $M \sim 2$ (Fig. 3). The horizontal wind speed upstream of the shock-like feature increases roughly from 200 m s^{-1} at 110 km to 300 m s^{-1} at 130 km (Figs. 1 and 2), while the upstream temperature roughly decreases from 200 K at 110 km to 100 K at 130 km, and then increases to 200 K at 140 km in the thermosphere. Therefore, as $M \propto \frac{\|\mathbf{v}\|}{\sqrt{T}}$, the largest impact on the Mach number upstream of the shock-like feature is the local minimum of temperature with altitude, located at 130 km.

This structure consisting of a shock-like feature above ~ 120 km, and adiabatic heating below, would be apparent in the temperature and density structures of horizontal profiles, but so far no such observation seems to exist. The nightside temperature maps measured by SPICAV on board VEx (Piccialli et al., 2015) are scattered, and their coverage is quite limited at the local times of the terminator structure, at 18–20 h and 4–6 h. Piccialli et al. (2015, figure 7) show a 15 K bump centered at 19 h at 115 km, but is much less than the variability of the nightside, as explained in the next section. Moreover, Clancy et al. (2015) retrieved supersonic cross-terminator zonal winds at 100 to 125 km, with faster winds in the evening than in the morning side, which is the case in our simulation at altitudes 130 km and above (Fig. 1).

4. Variability of the nightside dynamics

The time-averaged view of atmospheric fields in Section 3 does not show a crucial point of the GCM results: the strong variability of the nightside, in stark contrast to the quiet dayside, as seen in Figs. 6, 7, and 8. The SS–AS circulation on the dayside is very simply described as a time-independent increase of horizontal winds with solar zenith angle, modest temperature changes of less than 10 K at any location, and an almost constant atmospheric composition of 96% CO_2. Meanwhile, the nightside is subject to abrupt changes of atmospheric composition, horizontal wind velocity, vertical wind speed, and temperature on a timescale of tens of hours.

As SS–AS horizontal winds are decreased due to non-orographic gravity waves, a shock-like feature, and downward motion at the terminator, converging air flows form multiple local subsiding ~ 1000 km size eddies that vary in strength and location in a seemingly unstructured way. This behavior is apparent in the local maxima and minima of wind vorticity (e.g. at 130 km in Fig. 7), with those eddies on the nightside forming and disappearing in a matter of a few hours. The changes of horizontal wind speed induce a change in atmospheric composition. Indeed, CO_2 is photodissociated into O and CO on the dayside, and air depleted in CO_2 piles up wherever horizontal wind gets slower. CO_2 concentration thus varies in both local time and latitude (Fig. 6). Moreover, individual species start to diffuse separately according to their masses above the homopause due to molecular diffusion, leading to the prevalence of the lightest species, such as CO and O. Therefore, air composition is a tracer of dynamics on the

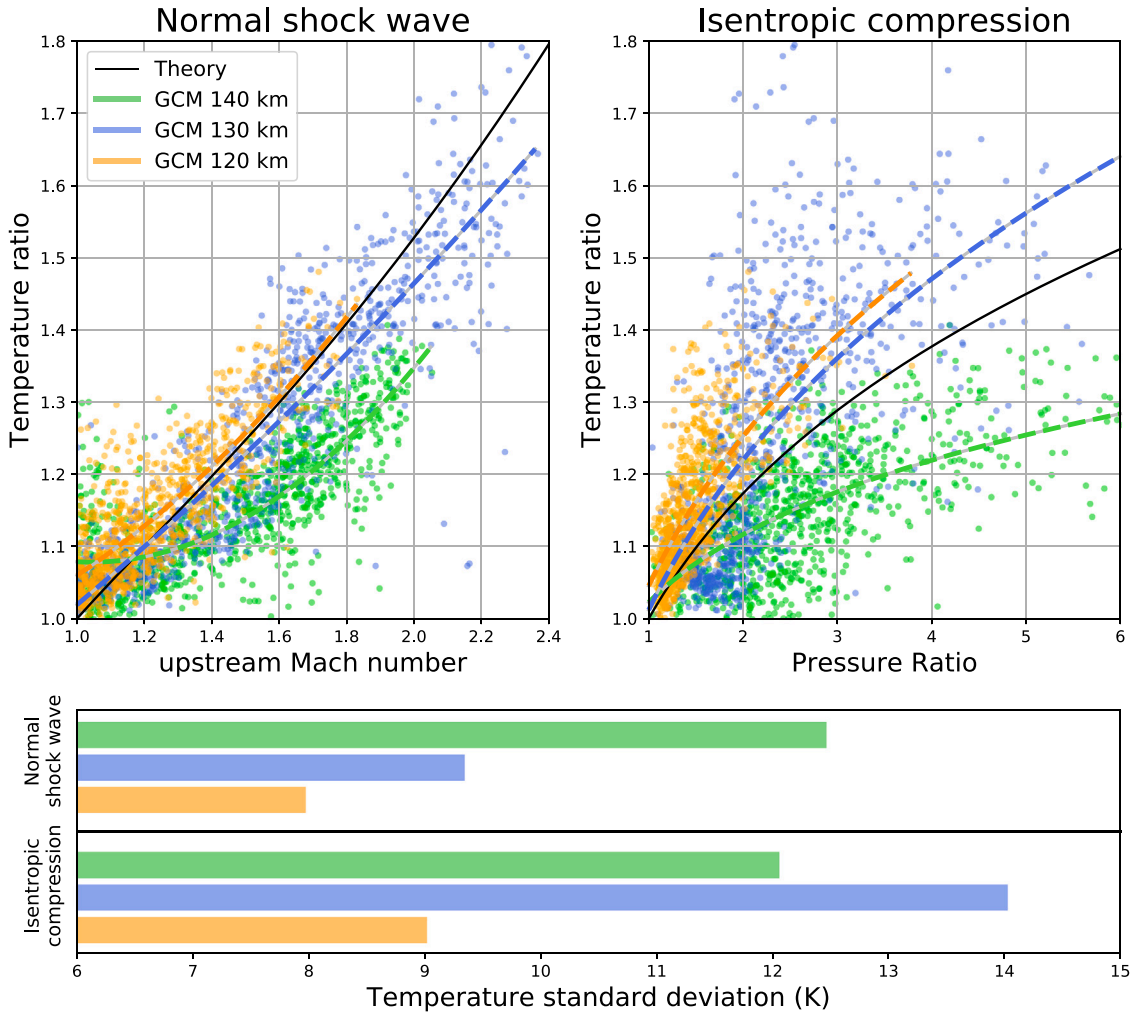


Fig. 5. Top: "Hot ring" temperature ratio as a function of upstream Mach number and pressure ratio. Black solid lines indicate the analytical 1-D normal shock equation given by Eq. (2) or the isentropic compression by Eq. (3). Dots indicate GCM values, and dashed color lines indicate the best fit to those values. Bottom: standard deviation between the GCM simulated temperature and Eqs. (2) and (3) for each case. The downstream (upstream) values are obtained for 10 Earth days from the locations of the local maximum (minimum) of temperature after (before) $M-1$ become negative along the SS–AS lines. (For interpretation of the references to color in this figure legend, the reader is referred to the web version of this article.)

nightside, with air composition and wind speed well correlated in Fig. 6. The varying vertical wind speed is well correlated locally with nightside temperatures, as the descending air is warmed by adiabatic compression in the region between the AS point and the hot ring caused by the shock-like feature (Fig. 8).

Such behavior of highly time-variable planetary scale structures on the nightside is not seen in simulations at lower resolution with the same GCM (Gilli et al., 2017), and was not reported with other GCMs (Brecht et al., 2011; Hoshino et al., 2012; Nakagawa et al., 2013), all having a lower resolution than the GCM simulation presented here. Fig. 9 compares the time-integrated eddy enstrophy q on the daysides and nightsides of simulations at low ($7.5° \times 5.625°$) and high ($3.75° \times 1.875°$) resolution with:

$$q(z) = \int_D |\nabla \times \mathbf{U}|^2 \, dS \tag{4}$$

with z the altitude and D the considered domain (e.g nightside or dayside). Eddy enstrophy is a useful quantity to assess eddy activity and the transience of the atmospheric flow. It gives a global metric of the wind vorticity and the associated energy per mass. The difference of eddy enstrophy by a factor 5 in Fig. 9 at altitudes 70 to 85 km between the two GCM resolutions is simply due to increased resolution that resolves more eddies. For the high resolution, eddy enstrophy above 90 km is seven times higher on the nightside than on the dayside. The difference between dayside and nightside eddy enstrophy increases to a factor 10 at 100 km for both resolutions, with a smaller spread, because the circulation of the dayside flow is direct and less variable than on the nightside. Above 110 km, the nightside enstrophy at high resolution does not vary much with altitude, whereas the low resolution one decreases by a factor around 3 between 110 and 130 km. The reason for such a difference between the two different resolutions is the presence of the shock-like feature above 110 km in the high-resolution case only, which reduces horizontal wind speeds and increases the number of large-scale eddies downstream of this shock-like feature. It is worth noting that eddy enstrophy is nearly constant with altitude above 100 km, so potential vorticity is not conserved, indicating a sink or source of potential vorticity from diabatic heating in the upper atmosphere, unlike the polar vortex at the cloud deck level (Garate-Lopez and Lebonnois, 2018).

Fig. 10 presents the periodograms of equatorial wind speed as a function of altitude and local time. There is a dominant 5.7 Earth days period at all altitudes above 40 km due to a Kelvin wave, as further explained in Section 5. Another period at 2.9 Earth days is also present at all those altitudes. The periodicity does not depend on local time in the lower atmosphere, in contrast with the transition and SS–AS regions. At 90 km, in the transition region, the atmospheric flow is more variable from midnight to noon, that is to say downstream to the AS

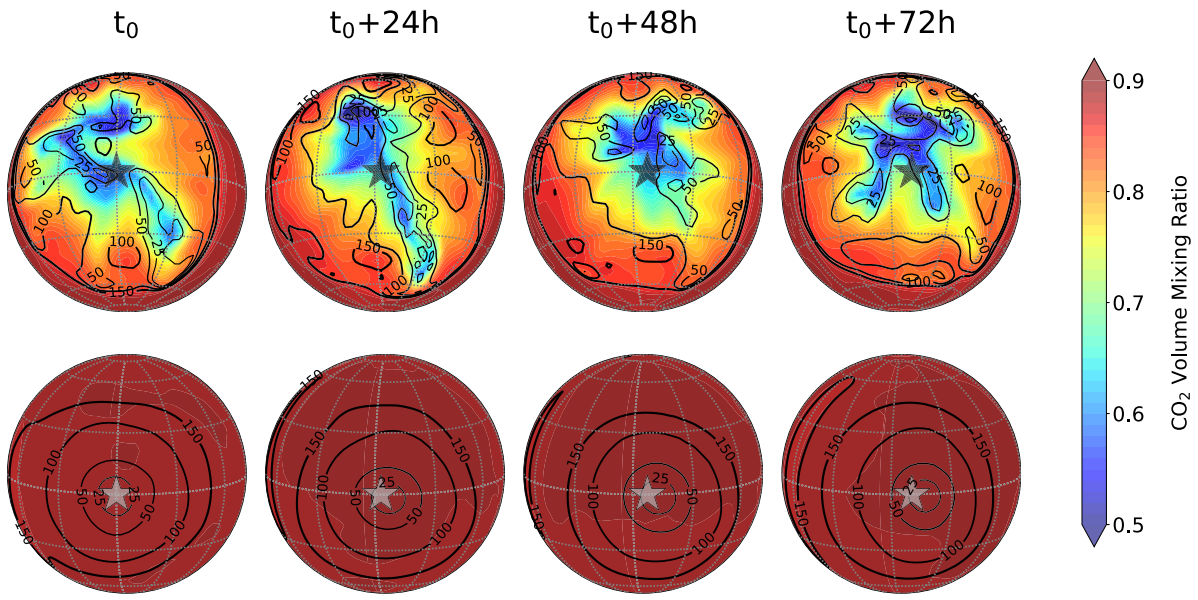


Fig. 6. Snapshots 24 h apart each of (colors) CO_2 in volume mixing ratio and (contour) wind speed in m s^{-1} at an altitude of 130 km for the (top) nightside and (bottom) dayside of Venus. The position of the subsolar point is indicated by a light gray star and the antisolar point by a dark gray star. (For interpretation of the references to color in this figure legend, the reader is referred to the web version of this article.)

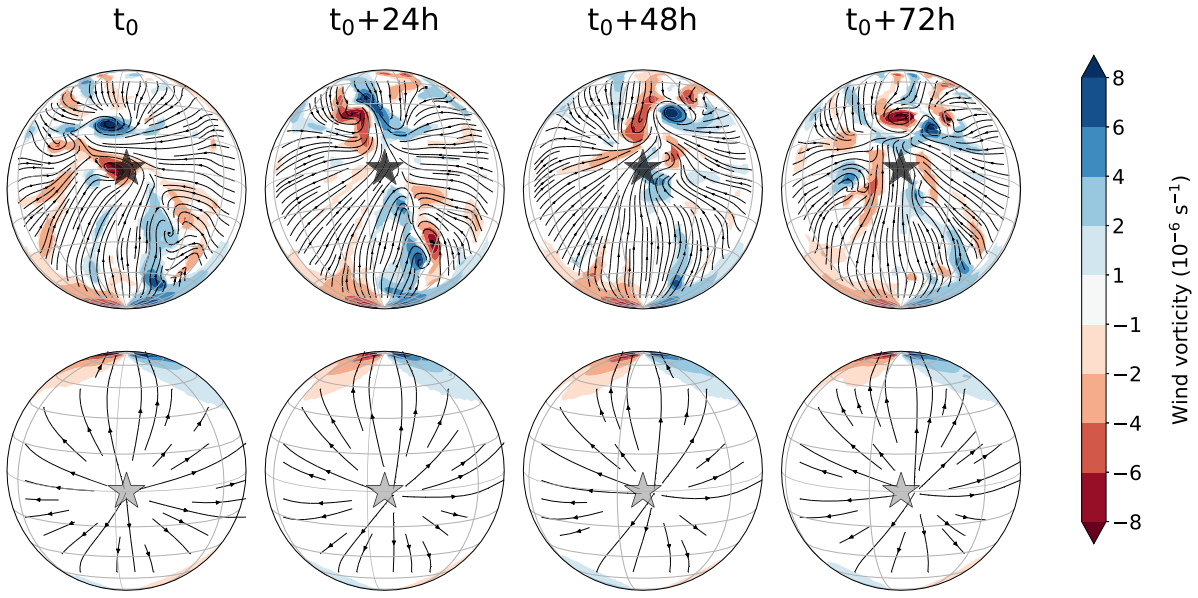


Fig. 7. Same as Fig. 6 with (colors) wind vorticity and wind streamlines at an altitude of 130 km for the (top) nightside and (bottom) dayside of Venus. (For interpretation of the references to color in this figure legend, the reader is referred to the web version of this article.)

point and below the inversion of zonal wind at the morning terminator (Figs. 1 and 3), than from noon to midnight, upstream of the AS point. Above 100 km, the local times for which the wind variability is greater are found between 0 h and 6 h. At 130 km, the whole nightside is variable, in contrast to a quieter dayside. The impact of the shock-like feature on wind variability is obvious at 130 km, with higher nightside variability clearly delimited at the location of the shock-like feature near the terminators. The 5.7-day period caused by the Kelvin wave is a major periodicity for all the atmospheric layers, but we could not assess if smaller frequencies would exist without it. In other words, it is not clear if the strong variability of the equatorial horizontal wind at high altitudes, and by extension of the upper atmosphere in general, requires this 5.7-day period from the lower atmosphere, or if it is an inherent characteristic of the nightside dynamics caused by the shock-like feature and downward motion.

5. Impact of the Kelvin wave

Kelvin waves in the Venusian atmosphere have been observed (e.g. Belton et al. (1976), Covey and Schubert (1982), del Genio and Rossow (1990)) and modeled (e.g. Yamamoto, 2019) on multiple occasions. Our simulation produces a westward propagating Kelvin wave excited in the middle and upper cloud deck, between 60 and 65 km. This Kelvin wave appears when a sufficiently strong zonal wind produces a Coriolis force for the local atmospheric flow (Peralta et al., 2015). The Kelvin wave may be linked to the meridional discontinuity observed in the lower cloud (Peralta et al., 2020). The detailed characteristics of this wave in the lower atmosphere are beyond the scope of this paper, but we can nevertheless briefly mention its main points. This wave also enters in resonance with a Rossby mode at mid-latitudes, forming a Kelvin–Rossby instability (Wang and Mitchell, 2014). Note

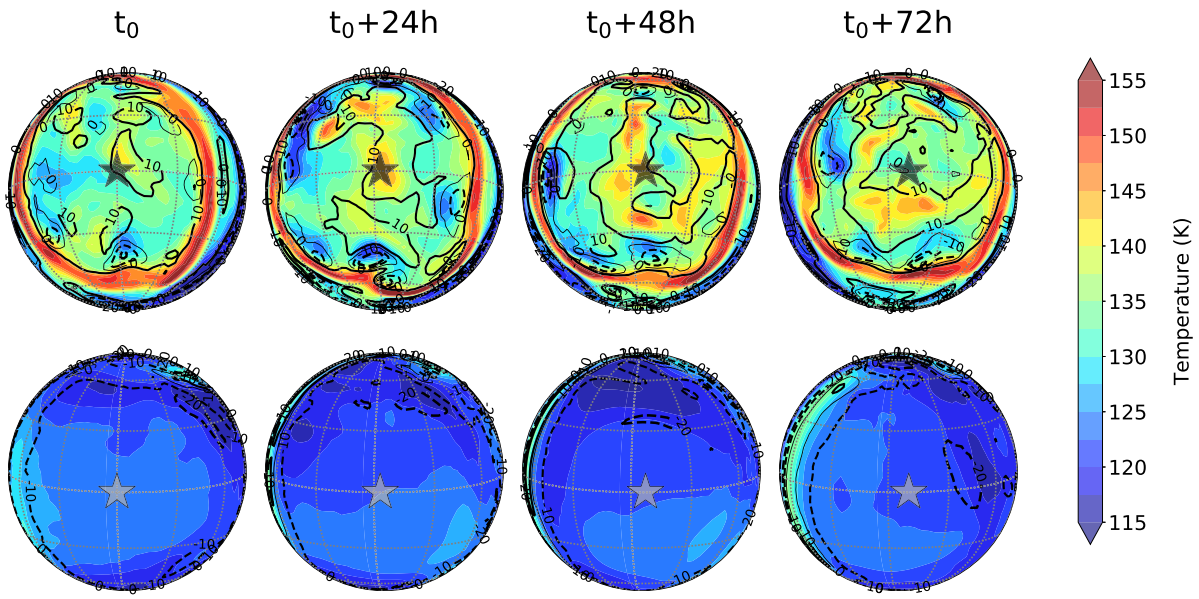


Fig. 8. Same as Fig. 6 with (colors) temperature and (contours) vertical wind speed (cm/s, downward positive) at an altitude of 120 km for the (top) nightside and (bottom) dayside of Venus. (For interpretation of the references to color in this figure legend, the reader is referred to the web version of this article.)

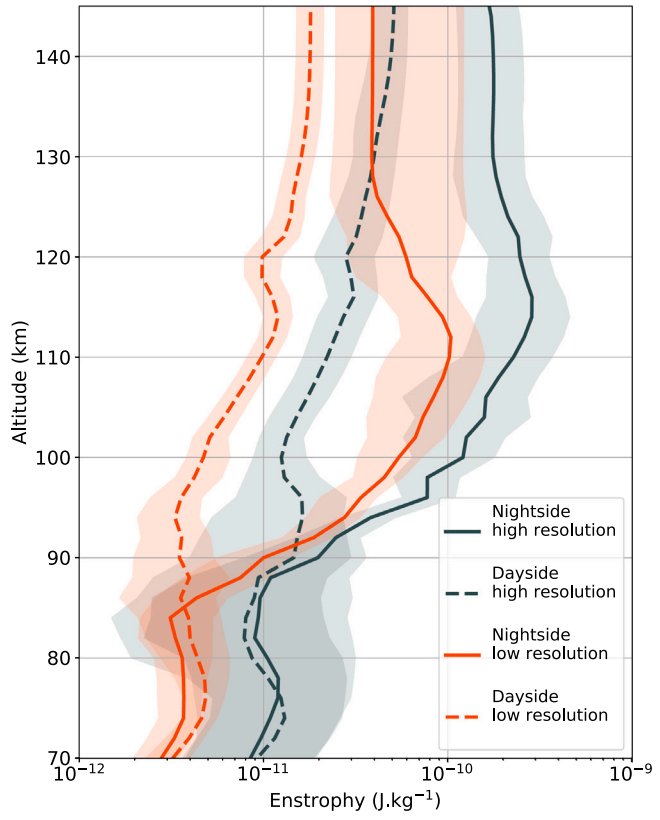


Fig. 9. Eddy enstrophy as a function of altitude averaged over 1 Vd and latitude lower than 75°, on the day and night sides, at high (96 × 96) and low (48 × 32) resolutions. The envelopes show the minima and maxima for 1 Vd.

that under Venusian conditions, and as it spans more than 100 km in altitude, the true nature of the wave we simulate is not straightforward, and may be a Kelvin-like, a Kelvin–Rossby type, or else. Therefore, we simply refer to it as a "Kelvin wave" and leave those considerations for further studies. When it reaches the cloud top, we note that the Kelvin wave has an average zonal wind amplitude of 5 m s^{-1} at 70 km and 15 m s^{-1} at 80 km (Fig. 11), and its latitudinal extent is 60°S to 60°N.

The period of this wave is 5.7 Earth days (Fig. 10) and depends on the zonal wind speed below the cloud deck. At the cloud top, this wave propagates slower than the mean zonal wind, while recent Akatsuki UV observations suggest that the Kelvin wave propagates faster (Imai et al., 2020). As our GCM underestimates the zonal wind speed at altitudes 30 to 40 km (Garate-Lopez and Lebonnois, 2018, Fig. 5), we would expect the period of the wave to be actually lower (Peralta et al., 2020). All in all, our simulated Kelvin wave's period and amplitude are in general agreement with observations of the cloud top (Imai et al., 2016; Imai et al., 2020), even if its period is too large, and if the morphology of the Y-feature is not apparent in the simulated zonal wind field at a fixed altitude or pressure. The absence of this feature could be due to the lack of a transported UV absorber in the GCM, that reveals such a spatial pattern in the observations (Peralta et al., 2015).

5.1. Impact on the upper atmosphere

The Kelvin wave has a considerable impact on both the transition region and the SS–AS circulation. The phase and amplitude structure of the equatorial zonal wind perturbed by the Kelvin wave is shown in Fig. 11. The wave has a wavenumber-1 structure up to roughly 95 km, and perturbs the wind field above and excites wind fluctuations that are seen with high amplitude on the nightside, but much less on the dayside (though they are still present). These fluctuations are excited by the wavenumber-1 Kelvin wave below 95 km, but do not keep this wavenumber-1 structure as they do not propagate upward the same way in the night and in the day. These perturbations are certainly secondary waves, excited by the Kelvin equatorial wave.

Therefore, the Kelvin wave is able to impact the SS–AS circulation except for local times close to noon. This result is contrary to the conclusion of analytical models, using idealized zonal wind vertical profiles of decreasing speed above the cloud top (Kouyama et al., 2015; Nara et al., 2020), that a Kelvin wave is attenuated below 80 km. Indeed, the structure of the zonal wind simulated by the IPSL VGCM is different, with speeds higher than 100 m s^{-1} on average in the transition region at the vicinity of the evening terminator (Fig. 1).

Brecht et al. (2021) prescribed Kelvin and Rossby waves-like perturbations in an upper atmosphere GCM with a lower boundary at 70 km, and found that the Kelvin wave propagate up to 110 km

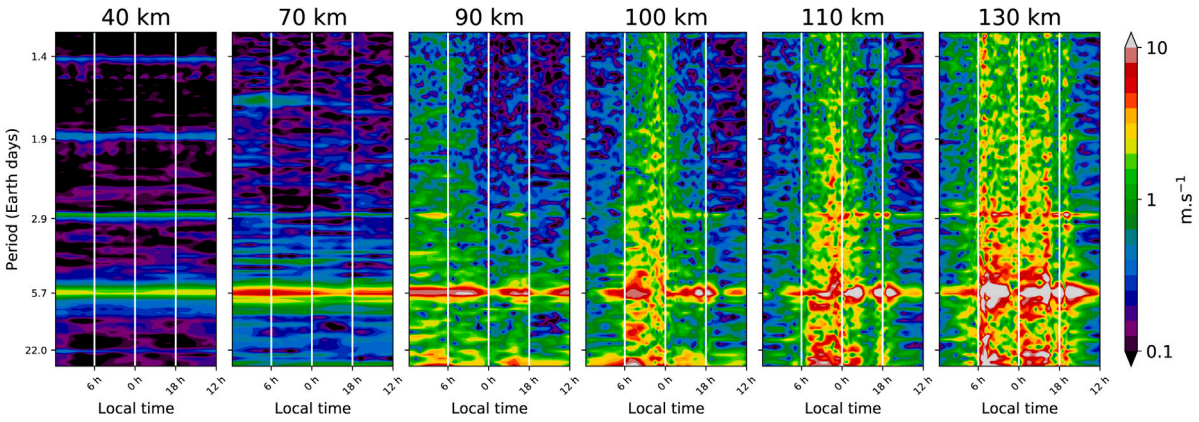


Fig. 10. Periodograms of equatorial (10°S-10°N) horizontal wind speed at different altitudes.

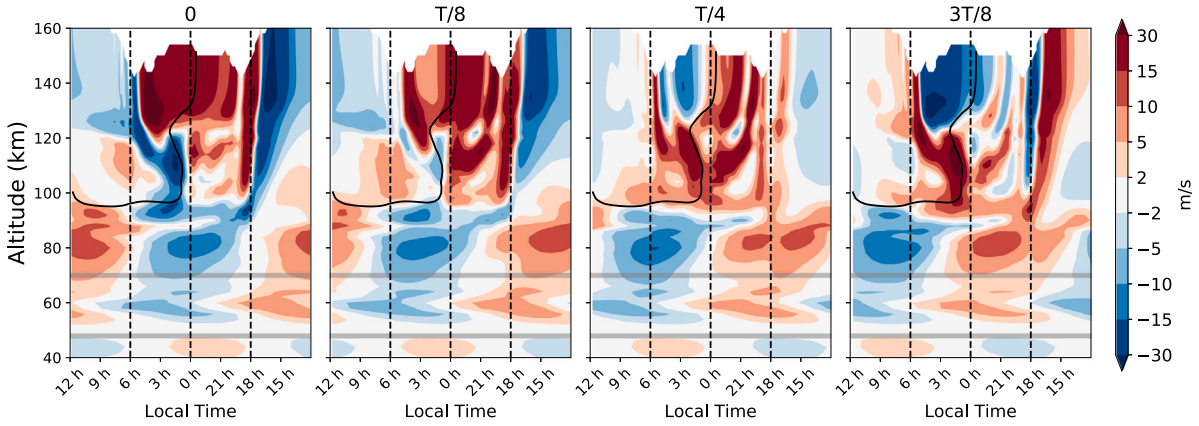


Fig. 11. Spectral decomposition of equatorial (10°S-10°N) zonal wind at frequency $2\pi/T$, with T = 5.7 Earth days, showing the westwards propagation and impact of the Kelvin wave for half of its period. The cloud bottom and top altitudes are indicated at 48 and 70 km. Thick solid line indicates where zonal wind values are zero on average. Upper and lower limits of the cloud deck are represented by two horizontal gray lines. The time zero is chosen as the cloud top maximum at local time 12 h.

only, due to differences with their vertical wind profile and amplitude and wavelength of their wave forcing, compared to the Kelvin wave naturally simulated in the IPSL GCM.

As a consequence of the resulting vertical profiles of horizontal wind, the zonal wind field impacted by the Kelvin wave in Fig. 11 is a complex structure, and is not straightforward to interpret. The vertical wavelength is 15 km in the lower and middle cloud deck, with an amplitude of 10 m s^{-1} (Peralta et al., 2020). In the upper cloud deck, the vertical wavelength dramatically changes, and is equal to 50 km, comparable to Hoshino et al. (2012). Downstream of the shock-like feature and downward motion on the nightside terminator, the zonal wind is 180° out-of-phase with the upstream side. This makes sense because in case of a shock, the faster a supersonic flow is, the slower the downstream subsonic flow is (c.f. Liepmann and Roshko, 2001). Another contribution to the out-of-phase structure on the nightside is the retrograde zonal flow entering from the transition region inside the region delimited by the shock-like feature, creating a temporary reversal of the SS–AS flow at 110 km with a delay of a few tens of hours. This reversal can be seen in the meridional wind structure of Fig. 12.

5.2. Impact on the nightside transition region

Fig. 12 shows the impact of the Kelvin wave on the meridional wind and oxygen species as the wave passes through the night. In the absence of a Kelvin wave, the SS–AS winds at 110 km are balanced in all directions, creating a convergence at the AS point. The Kelvin wave perturbs the zonal wind in the transition region below 95 km, creating a retrograde imbalance of the flow towards the morning side. As westwards wind rushes into the nightside from the evening terminator, two 2000 km large-scale transient vortices are formed in the transition region between local times midnight and 3 h, one in each hemisphere, as also seen in Fig. 15. As a consequence, a strong poleward transport attaining 150 m s^{-1} is present for approximately 100 h in both hemispheres, up to 60° latitude and 130 km of altitude. This causes the periodic transport of atomic oxygen to high latitudes after its downward transport. The location of the recombination of oxygen into $O_2(^1\Delta)$ thus happens at all latitudes from the equator to 60° in the transition region, with periodic episodes of high latitude 1.27 μm oxygen nightglow (Fig. 14).

5.3. Impact on the dayside SS-AS circulation

Similarly, Fig. 13 shows the impact of the Kelvin wave on the circulation and O species at 130 km of altitude. At this altitude, the Kelvin wave has a negligible impact on the zonal wind between local times 6 h and 15 h. Between 15 h and 18 h, the Kelvin wave creates a local maximum (minimum) of horizontal wind lasting approximately 100 h when the Kelvin wave cloud top zonal wind is minimum (maximum). This is shown in the panel at times 0 and 3T/8 of Fig. 11, with zonal wind maximum on the nightside in the RZS circulation, ducting into the dayside of the SS–AS circulation from the evening terminator. Then, the whole nightside is impacted by the Kelvin wave perturbation on the SS–AS evening branch, even if the Kelvin wave does not propagate into in the SS–AS morning branch between local times midnight to noon due to the zonal wind inversion at altitude 95 km. Since the cloud top zonal

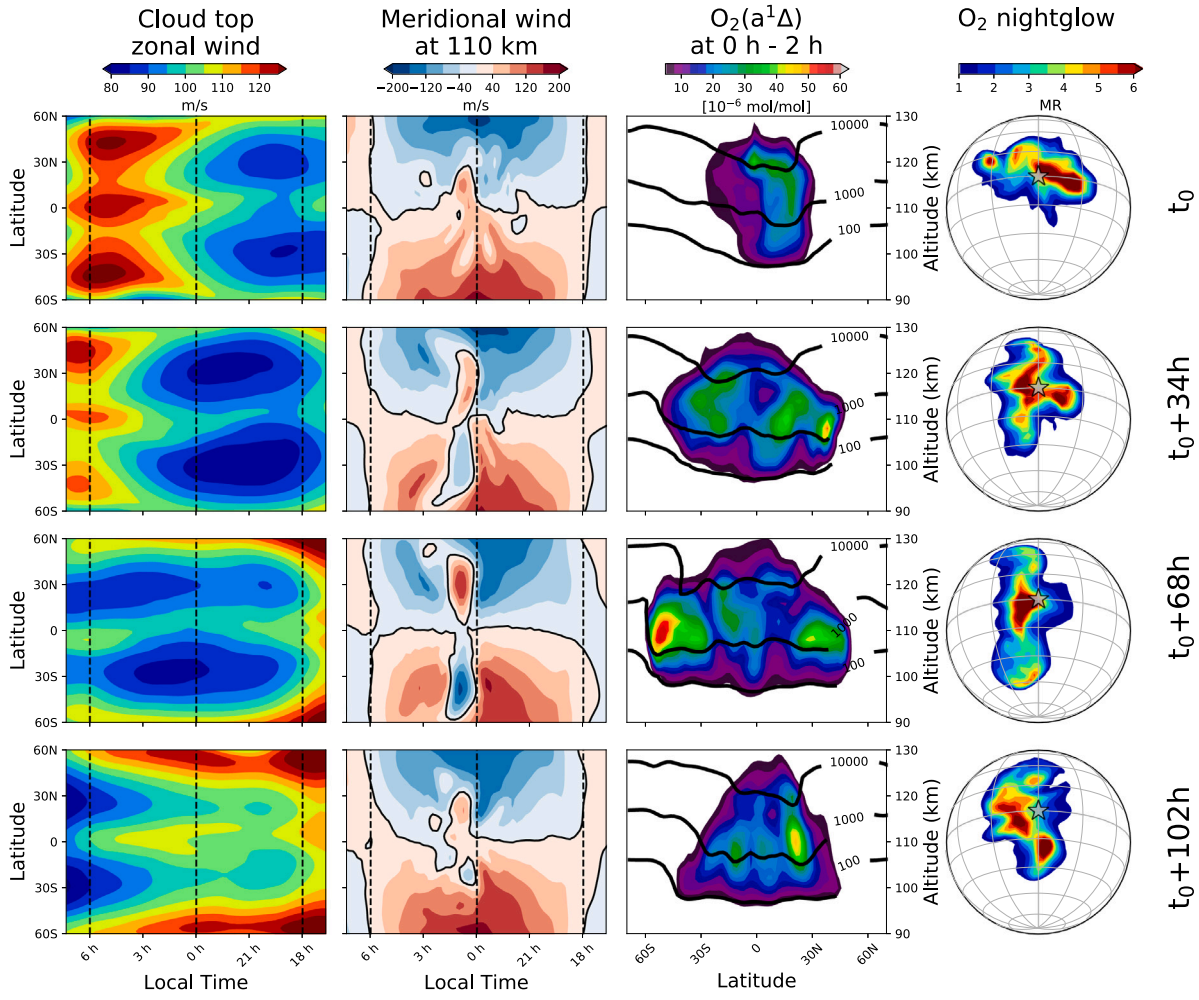


Fig. 12. Four consecutive snapshots, from left to right, of: (1) map of cloud top zonal wind, (2) map of meridional wind at 110 km, (3) latitude vs. altitude volume mixing ratio of $O_2(^1\Delta_g)$ (colors) and O (contours), (4) O_2 nightglow at 1.27 μm, with the AS point indicated by a gray star. (For interpretation of the references to color in this figure legend, the reader is referred to the web version of this article.)

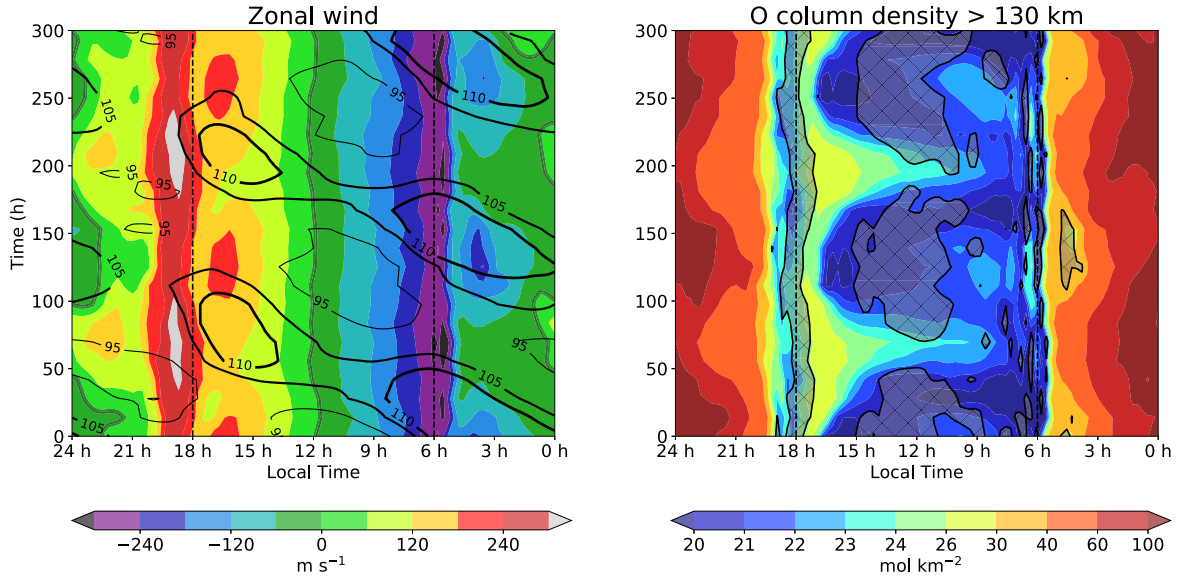


Fig. 13. Left: Equatorial zonal wind at 70 km (black contours) and 130 km (colors). Right: Column density of atomic oxygen for altitudes above 130 km (colors). Gray shaded areas indicate where the vertical wind is greater than 17 cm s^{-1} upwards at an altitude of 130 km. (For interpretation of the references to color in this figure legend, the reader is referred to the web version of this article.)

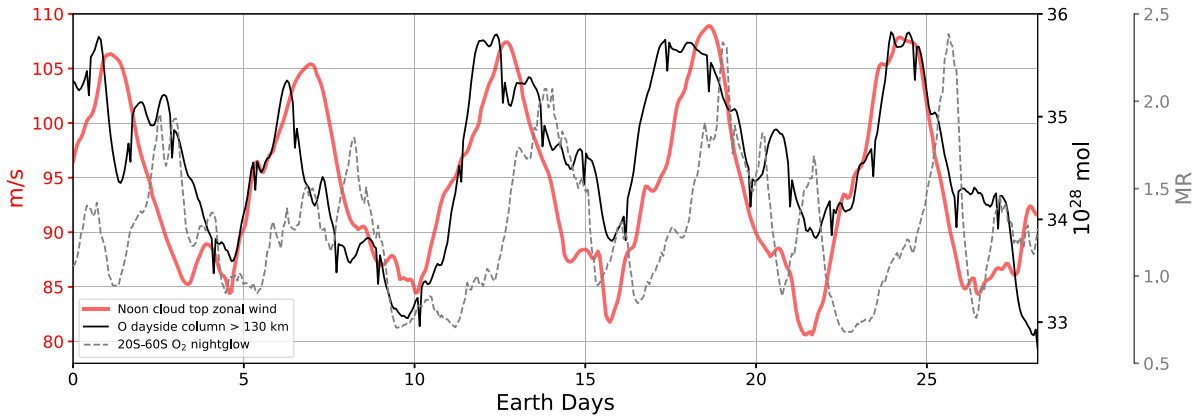


Fig. 14. Time series of noon cloud top zonal wind speed, dayside O column abundance above 130 km as a proxy for OI 135.6 nm dayglow, and O_2 nightglow at 1.27 μm at mid latitudes.

wind is maximum, the dayside SS–AS circulation is weakened, and thus the dayside upwards vertical wind is decreased (Fig. 13). Conversely, the upwards vertical wind is increased when the cloud top zonal wind is minimum. As can be seen in the right panel of Fig. 13, this increase of upwards motion, associated with a decrease of horizontal wind between 15 h and 18 h, favors a decrease of CO_2 abundance above 130 km, and an increase of O and CO abundances. Indeed, as explained in Section 3, the air composition at altitudes where CO_2 is being photodissociated depends on the local wind speeds. For instance, the vertically integrated column of O above 130 km, shown in Fig. 13, increases from 20 to 25 moles km^{-2}. All in all, CO_2 varies by 2000 ppm on the dayside due to the Kelvin wave, much less than the difference between the dayside and the nightside.

6. Oxygen airglows

The structure of the upper atmosphere and the impact of the Kelvin wave help us to understand the observations of two airglows: the emission of $O_2(^1\Delta)$ at 1.27 μm, and OI at 135.6 nm. We focus on these two airglows because they notably reveal the circulation at different local times and altitudes. Our GCM simulation provides new insights into the existing observations of these airglows. Other emissions have been observed, such as the nitric oxide UV nightglow (Stewart et al., 1980; Stiepen et al., 2013), OII 83.4 nm and OI 130.4 nm dayglows (Masunaga et al., 2015, 2017). However, the IPSL GCM does not yet include the nitrogen chemistry, and the OI emission at 130.4 nm is optically thick, making it difficult to interpret the O abundance (Masunaga et al., 2015).

6.1. O_2 ($^1\Delta$) nightglow

While O, O_2, and CO_2 are dynamical tracers computed online in the IPSL Venus GCM, the $O_2(^1\Delta)$ nightglow at 1.27 μm can be entirely calculated offline from the simulated GCM atmospheric fields. We employ the reaction rate coefficient k_1 of the trimolecular reaction $O + O + CO_2 \rightarrow O_2(^1\Delta) + CO_2$ given by Campbell and Gray (1973):

$$k_1 = 2.5 \times 9.4610^{-34} \exp\left(\frac{485}{T}\right) \quad (5)$$

with T the temperature. The volume emission rate VER (in photons.cm^{-3} s^{-1} = 10^{-4} kR km^{-1}) is calculated as:

$$\mathrm{VER} = \epsilon k_1 \frac{n_{co_2} n_o^2}{1 + \tau q n_{co_2}} \quad (6)$$

with n_{co_2} and n_o the concentration of CO_2 and O species in molecules.cm^{-3}, τ = 4470 s the Einstein coefficient, a quenching coefficient $q = 0.5 \times 10^{-20}$ cm^3 $molecule^{-1}$ s^{-1}, and ϵ the fraction of molecules produced in the $O_2(^1\Delta)$ state, rather than in higher excited states. This fraction is quite uncertain and may lie between 0.6 and 1. In his detailed discussion, Krasnopolsky (2011) recommended a value of 0.7. We adopted $\epsilon = 0.75$ for consistency with Gérard et al. (2009) and Soret et al. (2012). In this paper we present the nightside column integrated $O_2(^1\Delta)$ nightglow (Figs. 12, 15, and Appendix A), as it would be observed from nadir (Crisp et al., 1996; Lellouch et al., 1997; Hueso et al., 2008; Soret et al., 2012, 2014; Gorinov et al., 2018). On average, the nightglow is centered on the AS point. Still, the strong variability, detailed previously in Sections 4 and 5, creates a varied morphology of the nightglow's spatial structure. Nightglow intensity varies up to 12 MR in the vicinity of the AS point. Elongated structures up to 8 MR at mid-latitudes (30° to 60°) seen by Crisp et al. (1996) and Soret et al. (2014) are large-scale fronts created by the periodic poleward transport in the transition region triggered by the Kelvin wave, and associated with a 2000 km size vortex that varies on a daily timescale, as seen by Gérard et al. (2014). At lower latitudes, below 30°, highly variable bright spots are caused by eddies of subsiding flow whose location and intensity vary on a 10 h timescale.

6.2. OI 135.6 nm dayglow

OI 135.6 nm emission dayglow is produced by photoelectron impact in the upper atmosphere and is nearly proportional to O column density above 130 km (Masunaga et al., 2015; Nakamura et al., 2016). As explained in Section 5, the amount of atomic oxygen on the dayside is periodic and in phase with the cloud top noon zonal wind. Fig. 14 shows the time series of zonal wind and O dayside column as a proxy for the OI 135.6 nm dayglow. The total amount of dayside O is approximately 35×10^{28} moles above 130 km, with variations ranging from 2×10^{28} to 3×10^{28} moles, giving a variation of ~6 to ~8%. This value compares well to the ~4% variation of dayglow reported by Nara et al. (2020). The difference in observed and simulated variations may be explained by the fact that these observations were restricted to the morning side, and that the proportionality between O density and dayglow is sensitive to UV solar intensity. At the same time, we integrate the whole dayside with an average solar intensity in the GCM. Nara et al. (2020) reported a 3.6-day periodicity in both the dayglow and the cloud top zonal wind and Masunaga et al. (2015) a 4-day periodicity, while our model simulates a 5.7-day periodicity. This discrepancy stems from the atmospheric dynamics in the deep atmosphere in the cloud deck, since the Kelvin wave originates, as explained in Section 5. Artificially imposing more realistic faster winds in this region in the GCM results in a faster phase speed of the Kelvin wave (Peralta et al., 2020), as the Kelvin wave phase velocity depends on the zonal wind vertical profile (Peralta et al., 2015).

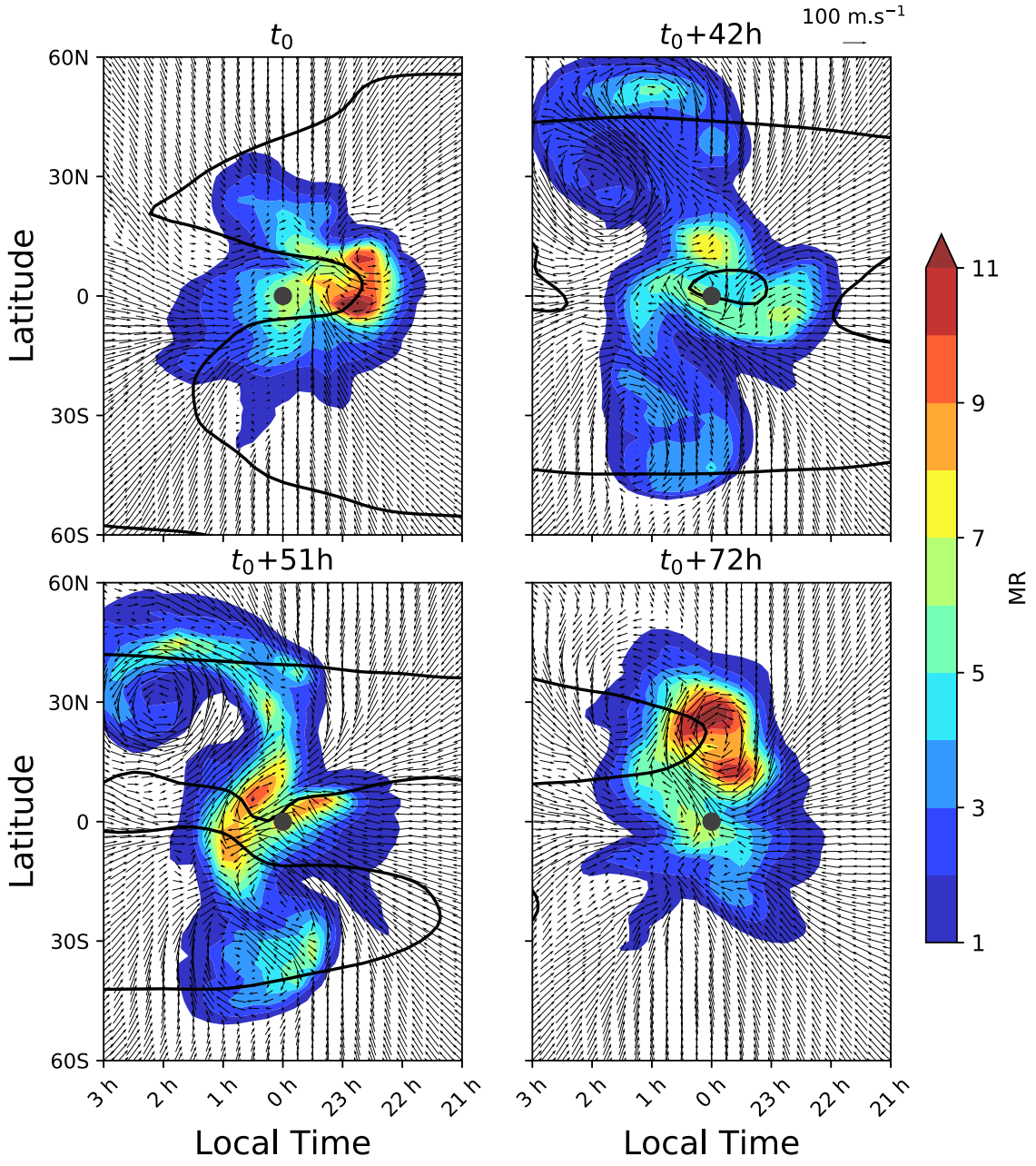


Fig. 15. 1.27 μm oxygen nightglow with wind arrows at 95 km. The black contours indicate the cloud top zonal retrograde wind at 100 m s^{-1} to show how the wind field is perturbed by the Kelvin wave underneath. See Appendix A for an animated version of this figure. (For interpretation of the references to color in this figure legend, the reader is referred to the web version of this article.)

6.3. Airglow intensities and cloud deck dynamics

Nara et al. (2020) reported and modeled a phase lag of 4 ± 2 h between the noon cloud top and the O dayglow intensity, and explained it as the sum of the times of vertical propagation of waves and diffusion of O. The mechanism revealed by our simulation does not let us determine on a phase lag. The complex pattern of wave propagation in the thermosphere (Fig. 11) is not entirely understood, while the analysis of simulated time series of zonal wind and O density suggest the absence of a phase lag between the noon cloud top and the O dayglow intensity (Fig. 14). The phase lag in the observations could be an artifact caused by uncertainties to the sensing altitude at the cloud top, and noise and sampling. Alternatively, the IPSL Venus GCM in its present form could inaccurately estimate a zero phase lag, due to inaccurate modeled background wind and temperature fields affecting the vertical propagation and impact of the Kelvin wave.

Interestingly, the same periodicity is also clearly visible in the O_2 nightglow emission at mid-latitudes, lagging behind the noon cloud top zonal maximum by approximately one-fourth of the Kelvin wave period, i.e. ~1.4 days. This phase lag is due to the phase lag of the Kelvin wave structure between the cloud top at the SS point, and the transition region at the AS point and the transport of O enriched air to high latitudes from the equator to mid-latitudes. The former is approximately one-eighth of the Kelvin wave period, as can be seen in the panel T/8 of Fig. 11, i.e. ~0.7 days. The latter corresponds to the transport of oxygen over from 30° to 50° latitude at ~80 m s^{-1} (Fig. 12), i.e. ~0.3 days. To our knowledge, no periodic behavior in the observations of the $O_2(^1\Delta)$ nightglow has ever been reported.

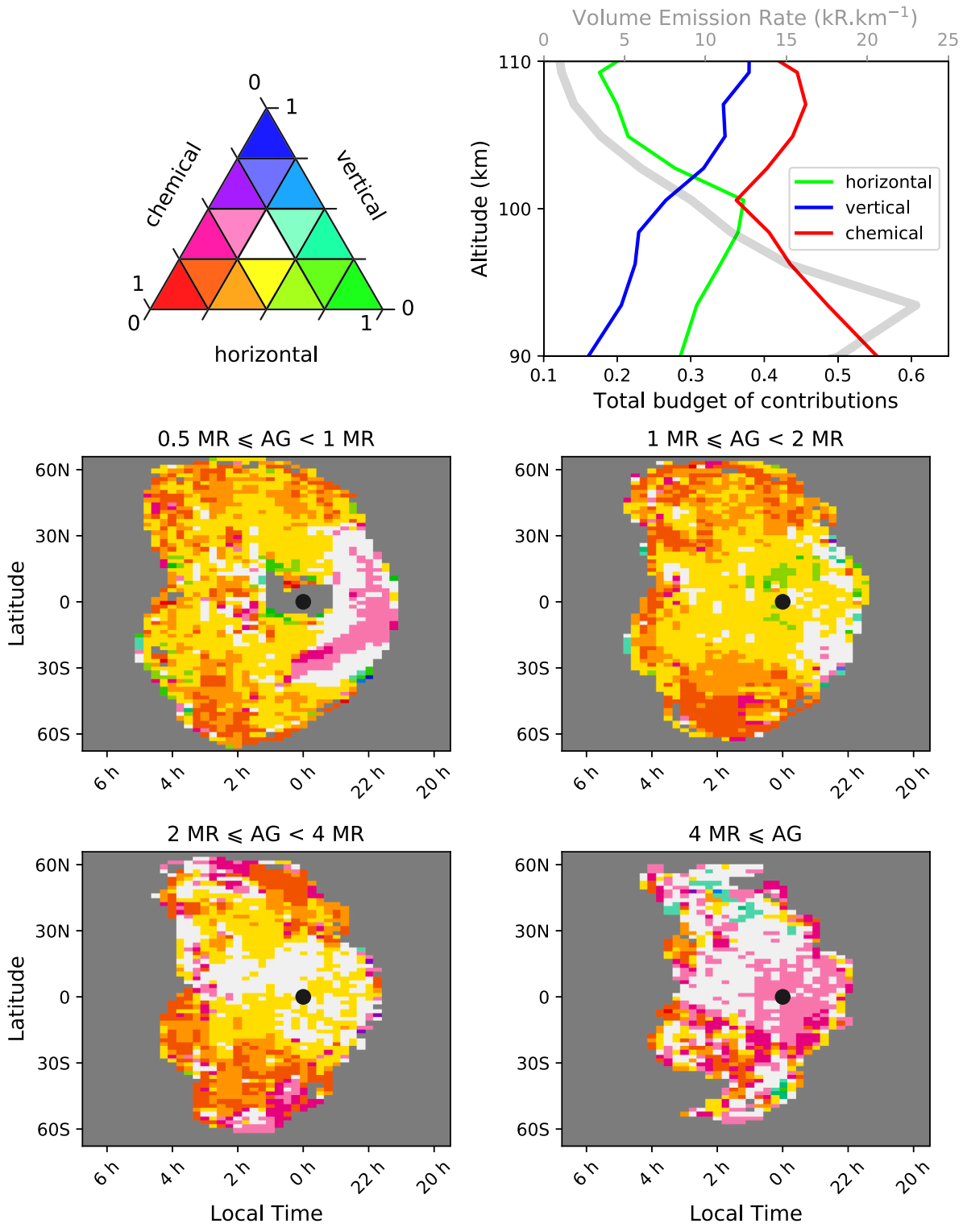


Fig. 16. Relative contributions of horizontal transport, vertical transport, and chemical reactions in the apparent motion of O_2 nightglow. AG stands for AirGlow column emission.

7. Interpreting nightglow's apparent motions

Hueso et al. (2008), Soret et al. (2014), and Gorinov et al. (2018) tracked the observed O_2 nightglow emission and derived its apparent horizontal motions. Variations of O_2 nightglow can be caused by horizontal transport, vertical transport, chemical reactions, or local change in temperature or density. Thus, the apparent motion is not necessarily equal to actual horizontal wind speeds, as hinted by Ohtsuki et al. (2008), who pointed out the importance of local strong downward flows on the O_2 nightglow. Therefore, how, when, and where the O_2 nightglow apparent motion is a good tracer of the atmospheric flow is a legitimate question. Since we benefit from a GCM able to simulate reasonably well the O_2 nightglow emission, the first model capable of reproducing the variability and high latitude events of observations, we aim to address this question.

A first look at Fig. 15 and associated animation (see Appendix A) reveals that large scale eddies play an important role in the nightglow apparent motion. $O_2(^1\Delta)$-enriched air is trapped inside downwelling eddies, and is every so often ejected from the eddy as it is disrupted or merges with other eddies. Those eddies are produced by the highly variable motion of flow past the shock-like feature in the thermosphere, and are subject to intense vertical downwards motion (Fig. 7), directly transporting atomic oxygen from higher altitudes, and eventually being a favored location of $O_2(^1\Delta)$ production. This could explain the bright emission patches observed by Ohtsuki et al. (2008), and seen and tracked in Soret et al. (2014), implying that their apparent motions reflect the eddy motion, rather than horizontal winds. Emission at high latitudes are caused by the poleward transport of O. Since this transport stops after a few tens of hours, the apparent motion at the front of the elongated structure is caused by the progressive lack of O available for recombination. This may have been observed by Gorinov et al. (2018), with elongated structures at high latitudes subject to a decrease of intensity at the end of the Kelvin wave cycle.

To quantify these behaviors, we computed the respective contributions from three terms responsible for the nightglow apparent motion: namely horizontal transport, vertical transport, and chemical reactions. Other terms, such as diffusion, are orders of magnitude smaller than these three terms. The apparent motion is related to the local change of the volume emission rate VER computed in Eq. (6):

$$\frac{d\mathrm{VER}}{d\mathrm{t}} = \left.\frac{\partial \mathrm{VER}}{\partial \mathrm{t}}\right|_{\mathrm{chem}} + \mathbf{U}\cdot\nabla\mathrm{VER} \tag{7}$$

with $\mathbf{U}$ the Eulerian wind. The chemical contribution is obtained from the recombination of atomic oxygen with rate coefficient k_1 from Eq. (5) for the source term, with inverse lifetime of $k_2 = 1/\tau = 1/4470\ s^{-1}$ (Lafferty et al., 1998) for the sink term:

$$\left.\frac{\partial \mathrm{VER}}{\partial \mathrm{t}}\right|_{\mathrm{chem}} = \epsilon k_1 n_{co_2} n_o^2 - k_2 n_{o_2(^1\Delta)} - q n_{o_2(^1\Delta)} n_{co_2} \tag{8}$$

Thus, the horizontal, vertical, and chemical contributions to $\frac{d\mathrm{VER}}{d\mathrm{t}}$, respectively noted h, v, and c, are computed as:

$$h = |U_x d_x \mathrm{VER} + U_y d_y \mathrm{VER}| \tag{9}$$

$$v = |U_z d_z \mathrm{VER}| \tag{10}$$

$$c = |\epsilon k_1 n_{co_2} n_o^2 - k_2 n_{o_2(^1\Delta)} - q n_{co_2} n_{o_2}| \tag{11}$$

with dx, dy, and dz the derivatives with respect to the x, y, and z directions.

The ratios $\frac{h}{h+v+c}$, $\frac{v}{h+v+c}$, and $\frac{c}{h+v+c}$, vertically weighted by VER, and averaged for four classes of total column intensity, are shown as maps in Fig. 16. On average, it is rare that one single contribution accounts for more than two-thirds of the total nightglow variation, meaning that, generally speaking, each of the three terms has comparable values. The vertical profiles for each contribution in Fig. 16 show that where the VER peaks near 95 km, the chemical contribution accounts for 50% of the VER variation, the horizontal transport for 30%, and the vertical one for 20%. Indeed, this altitude in the transition region is the major location of $O_2(^1\Delta)$ production and loss, while the nightside circulation is mostly horizontal. The vertical transport dominates the horizontal one above 100 km, with downward motion of the SS–AS circulation, and a peak of the relative abundance (volume mixing ratio) of $O_2(^1\Delta)$ in Fig. 12 near 110 km, higher than the VER peak at 95 km.

For nightglow emission < 1 MR, vertical transport dominates between local times 0 h and 22 h. At higher nightglow emissions, horizontal transport plays a dominant role. For nightglow emissions > 2 MR and more, the chemical contribution dominates at latitudes greater than 30°, as it corresponds to episodes of strong changes driven by the sudden influx or lack or atomic oxygen, such as the bright patches confined in eddies, or the high latitude episodes triggered by the Kelvin wave.

These results show that horizontal motions cannot alone explain the apparent motion of the fast changing nightglow in the complex circulation of the transition region, unlike clouds that act as mostly passive tracers, usually in quieter atmospheric flow. It does not mean that existing observations of nightglow apparent motion are necessarily poorly correlated with horizontal wind speeds. It rather means that apparent motion should be analyzed with caution, especially if such an analysis spans wide ranges of latitudes, local times, total emissions, morphology patterns, and Kelvin wave phases. For instance, manual tracking (Gorinov et al., 2018) discards features that are deformed or disappeared over short timescales, ensuring a crude, pragmatic, filtering that might select horizontal transport over vertical transport and chemical variations.

Interpreting nightglow apparent motion can greatly benefit from the outputs of such a GCM. Data assimilation would be an ideal technique for this feat, as it would optimally combine both the information given by observations and a GCM. It would be an interesting application to the emerging field of Venusian data assimilation (Sugimoto et al., 2017). Moreover, it could serve for the identification of possible GCM biases in the transition region, which is sensitive to both upper and lower atmosphere processes.

8. Discussion

Though we provided clues to long-standing scientific questions pertaining to Venus upper atmospheric circulation, some open questions remain nevertheless. These questions may be answered with further GCM studies with an emphasis on comparison between models, including data assimilation, as well as the analysis of existing observations and the planning of future ones:

8.1. Is there a supersonic shock in the Venusian upper atmosphere?

We provided evidence that the "hot ring" may indicate a shock, but the limitations of the dynamical core of the IPSL GCM currently only hints, but does not prove, that a shock may develop in the flow of the SS–AS circulation. The fact that the vertical component of sound waves are filtered out by the hydrostatic dynamical core probably hinders the modelling of the three dimensional structure of the shock-like feature. For instance, Fromang et al. (2016) found that vertical shear instabilities were leading to weak shocks in hot Jupiters. A shock-resolving code, applied to Venus, will answer the question of if and how a shock can actually form in its upper atmosphere.

One piece of the puzzle might be the measurements of cross-terminator supersonic winds by Clancy et al. (2015), showing a major unexplained characteristic: their high temporal variability, more than 100 m s^{-1} over an hourly timescale, with a fine limb resolution of ~0.2 h in local time, but a large horizontal resolution of 3000 km. They concluded that an unknown large-scale forcing mechanism must be invoked to account for these changes. Such a mechanism could be a moving shock, as it is a process that reduces wind speeds. Our simulations predict the Kelvin wave makes the shock-like feature position oscillate by ~0.5 h in local time on the evening, and ~0.2 h on the morning (left panel of Fig. 13). Thus, the measurements may have caught a shock passing through the limb, efficiently reducing wind velocity upstream.

8.2. What are the parameters controlling the characteristics of the Kelvin wave and the possible shock in the upper atmosphere?

The complex circulation modeled by the GCM creates waves that play a key role in atmospheric physical processes. However, under the complexity of the modeled waves (for instance the patterns of Fig. 11) and because of the lack of sufficient observational constraints, it not clear what controls some of their important characteristics, such as their amplitude, the location of the shock-like feature, the propagation

of secondary waves excited by the Kelvin wave at very high altitudes. This question shall be addressed by sensitivity analysis of the GCM and dedicated studies of the nonlinear theory applied to these waves in the Venusian context.

8.3. Can observations confirm that the O_2 nightglow spatially changing structure is linked to the Kelvin wave?

Although neither Crisp et al. (1996), Soret et al. (2014), nor Gorinov et al. (2018) reported any periodic behavior in the O_2 nightglow despite their long baselines, existing observations may prove sufficient to answer that question. A detailed analysis of VEx observations would confirm or disprove if the nightglow events seen by the VIRTIS-M imaging spectrometer are correlated with the Kelvin wave seen by the Venus Monitoring Camera (VMC) (Nara et al., 2019). This question is crucial, as it would put an observational constraint on the Kelvin wave structure in the upper atmosphere by observing at the same time the cloud top and the nightside transition region and providing a phase lag between the cloud top wind speed and the nightglow pulsation, if that pulsation were to actually exist.

8.4. What is the actual role of the non-orographic gravity waves on the nightside dynamics?

Many assumptions are made concerning this parameterization. Venus upper atmosphere GCMs that take into account non-orographic gravity waves suppose a uniform emission from the cloud top (Zalucha et al., 2013; Hoshino et al., 2012; Gilli et al., 2017), but our study shows how an increase of resolution is able to reveal the impact of structures nonexistent at a lower resolution. To explore this aspect, the use of a high-resolution mesoscale model (Lefèvre et al., 2020) or Large-Eddy Simulations (Imamura et al., 2014; Lefèvre et al., 2018) is poised to guide future GCM developments, as it did on Mars (e.g. Wang et al., 2018) and Earth.

8.5. What is the role of the planetary-scale mountain waves on the upper atmosphere?

The Akatsuki spacecraft found reoccurring planetary-scale mountain waves in the afternoon at five locations (Fukuhara et al., 2017; Kouyama et al., 2017). Our simulation did not include the mountain waves parameterization developed in Navarro et al. (2018) because it triggered a loss of angular momentum of nonphysical origin in the dynamical core on a 10 Vd timescale that would bring confusion in the analysis of the complex mechanisms at stake in the upper atmospheric circulation beyond the scope of this study. However, these mountain waves happen between noon and 18 h local time, and should extend into the SS–AS circulation in the absence of vertical shear. Thus, they may impact the evening terminator and how the Kelvin wave interacts with the shock-like feature, and in turn the nightside dynamics. However, Gorinov et al. (2018) claims a correlation between the structure of O_2 nightglow and its apparent motion with the underlying topography, which could perhaps be explained by a mechanism linked to mountain waves, as they are the only known manifestation of the topography on the cloud deck and above. Unexplained observations of small-scale fixed structures seen in the upper cloud deck's nightside and correlated with topography (Peralta et al., 2017), and large-scale cloud top varying speed (Bertaux et al., 2016) also exist.

8.6. What assumptions are valid for atmospheric retrievals?

In the light of the strong variability of atmospheric fields such as density, and temperature (Figs. 6 and 8), it may appear that assumptions made for existing observation retrievals are not always correct. We think that observations should be carefully retrieved, as air temperature and composition vary so much on a tens of hours timescale and hundreds of kilometers length-scale. For instance, the assumptions of spherical homogeneous layers (a.k.a. the onion-peeling technique) made for stellar (Piccialli et al., 2015) and solar (Vandaele et al., 2008; Mahieux et al., 2015) occultations may result in larger error bars than initially thought in the upper atmosphere. Moreover, the dependence of SOIR/SPICAV profiles based on an initial guess of CO_2 mixing ratio from the VTS3 semi-empirical model (Hedin et al., 1983) above 100 km, may not be correct and that it should be reflected in larger uncertainties in the region 100–140 km, where the VTS3 results are extrapolated. Once again, data assimilation may prove useful for the retrievals of observations made sufficiently frequent and consecutive to converge to an estimate of the true state of the atmosphere.

8.7. Can the different locations of He, and NO and O_2 nightglows be reconciled?

The shift of nitric oxide (NO) nightglow emission at 115 km towards the morning terminator formed by the reaction of atomic nitrogen and oxygen (Stewart et al., 1980; Stiepen et al., 2013) is difficult to interpret in terms of circulation because the peak of O_2 nightglow happens at midnight around 95 km. One essential difference between these nightglows is that the lifetime of N is at least one order of magnitude shorter than the one of O above 105 km (Collet et al., 2010). Elaborating on this fact, Collet et al. (2010) demonstrated that the peak emission of NO should happen ~10 h after injection of N and O, whereas the O_2 peak happens ~48 h after, thus suggesting that the NO nightglow is a better tracer of the dynamics than the O_2 one. Stewart et al. (1980), Bougher et al. (1990), Royer et al. (2010) and Stiepen et al. (2013) reported observations of variable NO nightglow in brightness and location, sharing the same characteristics as the O_2 nightglow, suggesting that both nightglows are subject to the complex variable dynamics of the transition region.

The IPSL Venus GCM does not include a nitrogen chemistry yet, so it cannot simulate the NO species. However, some general considerations can be made from the simulation results. Even though the average zonal wind is zero, the asymmetry in the circulation seen in Fig. 1 could perhaps explain the NO maximum at 110 km, since the circulation on the morning terminator could trap species at an altitude of ~100 km. Between about 100 and 130 km, the zonal wind convergence is shifted westward from the AS-point, between midnight and 2 h. One possible source of O and N in the NO production could be their photodissociation on the dayside between 100 and 120 km, and transported to the nightside downwards, west of the AS point. This would be in contrast to the source of O for the creation of O_2, with O coming mainly from photodissociation above 130 km and transported downwards to the AS point. These two different source locations and transport paths would favor faster chemical processes in the first case with NO, and longer ones in the second case with O_2.

Regarding the He nightglow, although the maximum of this emission is located at 165 km, above the top of our model, our current simulations cannot interpret the emission shift towards the morning terminator (Brinton et al., 1980) as an effect of superrotation. Instead, we suggest it might be caused by the indirect impact of the Kelvin wave on the nightside, periodically transporting helium westward, or an external effect such as an asymmetry of the solar wind in the Venus frame of Lundin et al. (2011). Thus, the nightside westward shift of both nitric oxide and helium at different altitudes does not necessarily point to a common mechanism, and future development of the IPSL VGCM (inclusion of the chemistry of nitrogen and vertical extension up to the ionosphere) may shed light on this topic.

9. Conclusion

Our simulation of the ground-to-thermosphere Venusian circulation with the IPSL Venus GCM reveals unexpected features, such as a shock-like feature in the SS–AS circulation near the terminator (manifested

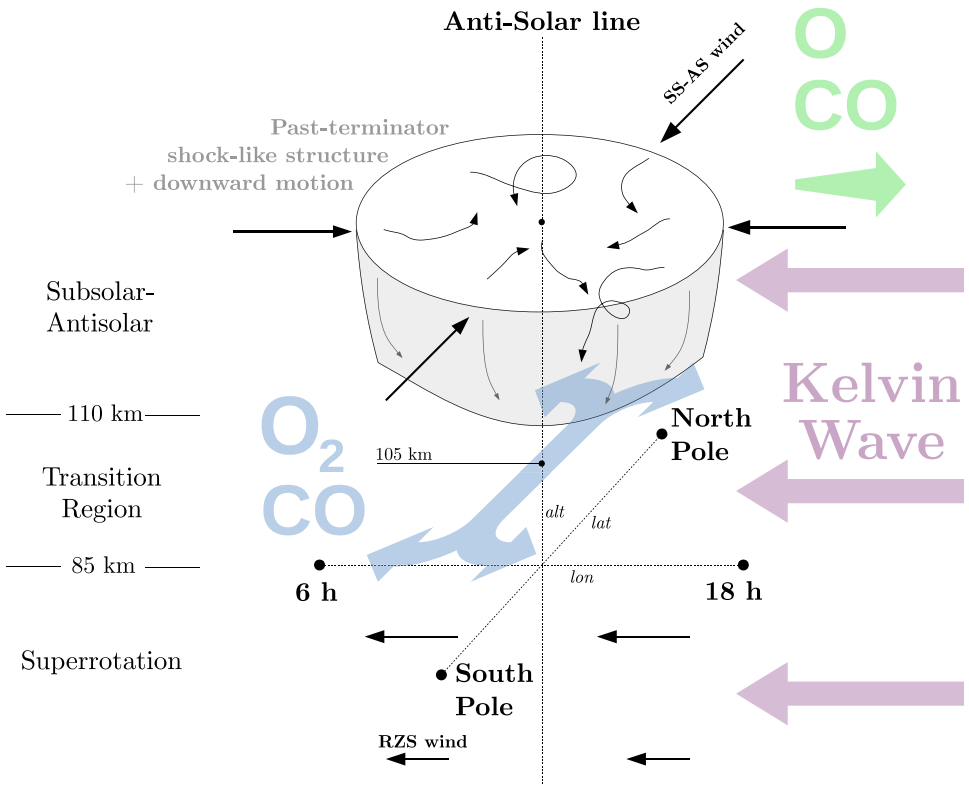


Fig. 17. Principal mechanisms of the upper atmospheric circulation from the IPSL VGCM. Supersonic wind speeds create a shock and downward motion at the terminator, with reduced speed and CO_2 depleted air downstream. The Kelvin wave periodically transports O_2 and CO poleward in the nightside transition region, and enhances dayside O and CO abundances.

by a Lamb wave due to the hydrostatic dynamic core), and a direct intrusion of a sub-cloud Kelvin wave to the upper atmosphere. Our proposed mechanism, summed up in Fig. 17, invokes these mechanisms to explain the variability the nightside upper atmosphere and the characteristics of the IR O_2 and EUV O airglows observations. Note that CO is also periodically transported to high latitudes in the transition region as O_2 is, and enhanced on the dayside of the thermosphere as O is.

This simulation gives new insights on processes occurring in the upper atmosphere of Venus. However, it remains a pure modeling study that comes with limitations, known and unknown. We can identify some possible limitations to the realism of the simulation:

- The accuracy of the upward propagation of the Kelvin wave and its secondary waves impacting the upper atmosphere is a critical component of the model and for the results presented here. The wave's vertical propagation strongly depends on the simulated wind and temperature fields. The Kelvin wave is naturally occurring by the IPSL GCM, unlike forced waves above the cloud deck in GCMs that do not include the lower atmosphere (Hoshino et al., 2012; Brecht et al., 2021). On one hand, this capability is an asset of our GCM, since it creates a wave forcing thought to be as realistic as possible. On the other hand, this could also be seen as a limitation because assessment of the upper atmosphere's sensitivity to wave characteristics is made difficult, requiring sophisticated changes in the simulated global wind and temperature fields.
- The non-orographic gravity wave drag parameterization assumes a homogeneous source of small scale gravity waves from the top of convective cells (~55 km). The source may actually vary with time and latitude. Other unresolved gravity waves from the low stability regions on the day and night sides of the upper atmosphere (Fig. 1) may also play a role in the circulation. This would require a combination of high resolution mesoscale and Large Eddy Simulations (LES) for both the cloud deck (Lefèvre et al., 2018, 2020) and the upper atmosphere. This is important because it impacts the strength of the SS–AS circulation, and in turn the location of the shock wave near the terminator. For instance, enhanced winds would push the shock closer to the AS point and reduce the horizontal extent of the region with variable dynamics on the nightside. This is what we notice when we turn off this parameterization. A weakened shock would let more westwards flow enter the nightside, triggering a more vigorous subsidence and poleward transport. This is also what we noted during the first few Venus solar days of simulation before convergence, with O_2 nightglow reaching the pole during Kelvin wave events, while it is limited to 60° once the circulation is established.
- Mountain waves described in Fukuhara et al. (2017), Kouyama et al. (2017) and Navarro et al. (2018) are not included in the simulation presented here. One reason is that they destroy the superrotation through nonphysical non-conservation of angular momentum in the dynamical core as explained in Lebonnois et al. (2012) and Navarro et al. (2018). They would reduce zonal winds below and inside the cloud deck, drastically changing the Kelvin wave over the course of tens of Venus days that are necessary to reach a steady circulation in the upper atmosphere. As mountain waves occur between noon and 18 h, they may impact the circulation at the evening terminator, and in turn the whole nightside dynamics.
- There is a clear gap in the results by changing the resolution from 46 × 32 to 96 × 96. For that matter, we recommend that any Venus upper atmospheric GCM should test if there is a threshold in resolution that creates a shock-like structure, i.e a sharp decrease of horizontal winds followed by sudden warming and increase in pressure and density. However, other similar behaviors with threshold in resolution may exist when increasing further the resolution, by resolving smaller scale waves that would alter the structure of the nightside dynamics.

- The UV solar flux assumes a mean solar condition for the eight years of the VEx mission, from 2006 to 2014 (Gilli et al., 2017). Therefore, the simulation is not sensitive to the 11-year solar cycle. The bigger impact is on the EUV heating on the dayside above 130 km, responsible for higher dayside temperatures, and a driver of the SS–AS circulation. An increase of this forcing may result in a change in SS–AS wind speeds near the terminator, and in turn the location of the shock and downward flow on the nightside. Interestingly, Soret and Gérard (2015) found no evidence of correlation between O_2 nightglow emission and solar activity during the VEx mission. Simulations with a different level of solar activity have not been conducted yet and are a topic of future research.

Finally, this work is part of a growing list of evidences that the deep atmospheric dynamics directly impacts the whole atmosphere up to the thermosphere, with numerous observables exhibiting periodicities associated with superrotation. Since Venus is a laboratory for terrestrial exoplanets with slow rotation and strong insolation gradient leading to a vigorous day-to-night circulation (Kane et al., 2019), typically planets orbiting M-dwarfs, this result may prove of interest to the interpretation of observations of exoplanetary atmospheres.

Acknowledgments

TN and GS acknowledge NASA Akatsuki Participating Scientist Program under grant NNX16AC84G. GG was supported by the European Union's Horizon2020 research and innovation programme under the Marie Sklodowska-Curie grant agreement No 796923 and by Fundação para a Ciência e a Tecnologia (FCT) through the research grants UIDB/04434/2020, UIDP/04434/2020, P-TUGA PTDC/FIS-AST/29942/2017. SL acknowledges the support of the Centre National d'Études Spatiales (CNES). This work used computational and storage services associated with the Hoffman2 Shared Cluster provided by UCLA Institute for Digital Research and Education's Research Technology Group, as well as the High-Performance Computing (HPC) resources of Centre Informatique National de l'Enseignement Suérieur (CINES) under the allocations A0060110391 and A0080110391 made by Grand Equipment National de Calcul Intensif (GENCI).

Appendix A. Supplementary data

Supplementary material related to this article can be found online at https://doi.org/10.1016/j.icarus.2021.114400.

References

Ando, H., Sugimoto, N., Takagi, M., Kashimura, H., Imamura, T., Matsuda, Y., 2016. The puzzling Venusian polar atmospheric structure reproduced by a general circulation model. Nature Commun. 7, 10398. http://dx.doi.org/10.1038/ncomms10398.

Belton, M.J.S., Smith, G.R., Schubert, G., del Genio, A.D., 1976. Cloud patterns, waves and convection in the Venus atmosphere. J. Atmos. Sci. 33, 1394–1417. http://dx.doi.org/10.1175/1520-0469(1976)033<1394:CPWACI>2.0.CO;2.

Bertaux, J.-L., Khatuntsev, I.V., Hauchecorne, A., Markiewicz, W.J., Marcq, E., Lebonnois, S., Patsaeva, M., Turin, A., Fedorova, A., 2016. Influence of venus topography on the zonal wind and UV albedo at cloud top level: The role of stationary gravity waves. J. Geophys. Res. (Planets) 121 (6), 1087–1101. http://dx.doi.org/10.1002/2015JE004958.

Bertaux, J.-L., et al., 2007. A warm layer in venus' cryosphere and high-altitude measurements of HF, HCl, H_2O and HDO. Nature 450 (7170), 646–649. http://dx.doi.org/10.1038/nature05974.

Bougher, S.W., Alexander, M.J., Mayr, H.G., 1997. Upper atmosphere dynamics: Global circulation and gravity waves. In: Bougher, S.W., Hunten, D.M., Phillips, R.J. (Eds.), Venus II: Geology, Geophysics, Atmosphere, and Solar Wind Environment. p. 259.

Bougher, S.W., Dickinson, R.E., Ridley, E.C., Roble, R.G., 1988a. Venus mesosphere and thermosphere III. Three-dimensional general circulation with coupled dynamics and composition. Icarus 73 (3), 545–573. http://dx.doi.org/10.1016/0019-1035(88)90064-4.

Bougher, S.W., Dickinson, R.E., Ridley, E.C., Roble, R.G., Nagy, A.F., Cravens, T.E., 1986. Venus mesosphere and thermosphere II. Global circulation, temperature, and density variations. Icarus 68 (2), 284–312. http://dx.doi.org/10.1016/0019-1035(86)90025-4.

Bougher, S.W., Gerard, J.C., Stewart, A.I.F., Fessen, C.G., 1990. The Venus nitric oxide night airglow: Model calculations based on the Venus thermospheric general circulation model. J. Geophys. Res. 95 (A5), 6271–6284. http://dx.doi.org/10.1029/JA095iA05p06271.

Brecht, A.S., Bougher, S.W., 2012. Dayside thermal structure of Venus' upper atmosphere characterized by a global model. J. Geophys. Res. (Planets) 117 (E8), E08002. http://dx.doi.org/10.1029/2012JE004079.

Brecht, A.S., Bougher, S.W., Gérard, J.C., Parkinson, C.D., Rafkin, S., Foster, B., 2011. Understanding the variability of nightside temperatures, NO UV and O_2 IR nightglow emissions in the Venus upper atmosphere. J. Geophys. Res. (Planets) 116 (E8), E08004. http://dx.doi.org/10.1029/2010JE003770.

Brecht, A.S., Bougher, S.W., Shields, D., Liu, H.L., 2021. Planetary-scale wave impacts on the venusian upper mesosphere and lower thermosphere. J. Geophys. Res. (Planets) 126 (1), e06587. http://dx.doi.org/10.1029/2020JE006587.

Brinton, H.C., Taylor, H.A., Niemann, H.B., Mayr, H.G., Nagy, A.F., Cravens, T.E., Strobel, D.F., 1980. Venus nighttime hydrogen bulge. Geophys. Res. Lett http://dx.doi.org/10.1029/GL007i011p00865.

Campbell, I.M., Gray, C.N., 1973. Rate constants for $O(^3P)$ recombination and association with $N(^4S)$. Chem. Phys. Lett. 18 (4), 607–609. http://dx.doi.org/10.1016/0009-2614(73)80479-8.

Clancy, R.T., Sandor, B.J., Hoge, J., 2015. Doppler winds mapped around the lower thermospheric terminator of Venus: 2012 solar transit observations from the James Clerk Maxwell Telescope. Icarus 254, 233–258. http://dx.doi.org/10.1016/j.icarus.2015.03.031.

Clancy, R.T., Sandor, B.J., Moriarty-Schieven, G.H., 2008. Venus upper atmospheric CO, temperature, and winds across the afternoon/evening terminator from June 2007 JCMT sub-millimeter line observations. Planet. Space Sci. 56 (10), 1344–1354. http://dx.doi.org/10.1016/j.pss.2008.05.007.

Clancy, R.T., Sandor, B.J., Moriarty-Schieven, G., 2012. Thermal structure and CO distribution for the Venus mesosphere/lower thermosphere: 2001–2009 inferior conjunction sub-millimeter CO absorption line observations. Icarus 217 (2), 779–793. http://dx.doi.org/10.1016/j.icarus.2011.05.032.

Collet, A., Cox, C., Gérard, J.-C., 2010. Two-dimensional time-dependent model of the transport of minor species in the Venus night side upper atmosphere. Planet. Space Sci. 58 (14–15), 1857–1867. http://dx.doi.org/10.1016/j.pss.2010.08.016.

Covey, C., Schubert, G., 1982. Planetary-scale waves in the Venus atmosphere. J. Atmos. Sci. 39, 2397–2413. http://dx.doi.org/10.1175/1520-0469(1982)039<2397:PSWITV>2.0.CO;2.

Crisp, D., 1986. Radiative forcing of the venus mesosphere I. Solar fluxes and heating rates. Icarus 67 (3), 484–514. http://dx.doi.org/10.1016/0019-1035(86)90126-0.

Crisp, D., Meadows, V.S., Bézard, B., de Bergh, C., Maillard, J.P., Mills, F.P., 1996. Ground-based near-infrared observations of the Venus nightside: 1.27-μm $O_2(a\Delta_g)$ airglow from the upper atmosphere. J. Geophys. Res.: Planets 101 (E2), 4577–4594. http://dx.doi.org/10.1029/95JE03136.

del Genio, A.D., Rossow, W.B., 1990. Planetary-scale waves and the cyclic nature of cloud top dynamics on Venus. J. Atmos. Sci. 47, 293–318. http://dx.doi.org/10.1175/1520-0469(1990)047<0293:PSWATC>2.0.CO;2.

Dickinson, R.E., Ridley, E.C., 1972. Numerical solution for the composition of a thermosphere in the presence of a steady subsolar to-antisolar circulation with application to venus. J. Atmos. Sci. 29 (8), 1557–1570. http://dx.doi.org/10.1175/1520-0469(1972)029<1557:NSFTCO>2.0.CO;2.

Dickinson, R.E., Ridley, E.C., 1975. A numerical model for the dynamics and composition of the Venusian thermosphere. J. Atmos. Sci. 32, 1219–1231. http://dx.doi.org/10.1175/1520-0469(1975)032<1219:ANMFTD>2.0.CO;2.

Dickinson, R.E., Ridley, E.C., 1977. Venus mesosphere and thermosphere temperature structure. II. Day-night variations. Icarus 30 (1), 163–178. http://dx.doi.org/10.1016/0019-1035(77)90130-0.

Didion, A., Komjathy, A., Sutin, B., Nakazono, B., Karp, A., Wallace, M., Lantoine, G., Krishnamoorthy, S., Rud, M., Cutts, J., et al., 2018. Remote sensing of venusian seismic activity with a small spacecraft, the VAMOS mission concept. In: 2018 IEEE Aerospace Conference. IEEE, pp. 1–14. http://dx.doi.org/10.1109/AERO.2018.8396447.

Drossart, P., et al., 2007. A dynamic upper atmosphere of Venus as revealed by VIRTIS on Venus Express. Nature 450 (7170), 641–645. http://dx.doi.org/10.1038/nature06140.

Eymet, V., Fournier, R., Dufresne, J.L., Lebonnois, S., Hourdin, F., Bullock, M.A., 2009. Net exchange parameterization of thermal infrared radiative transfer in Venus' atmosphere. J. Geophys. Res. (Planets) 114 (E11), E11008. http://dx.doi.org/10.1029/2008JE003276.

Fromang, S., Leconte, J., Heng, K., 2016. Shear-driven instabilities and shocks in the atmospheres of hot Jupiters. Astron. Astrophys. 591, A144. http://dx.doi.org/10.1051/0004-6361/201527600, arXiv:1603.02794.

Fukuhara, T., Futaguchi, M., Hashimoto, G.L., Horinouchi, T., Imamura, T., Iwagaimi, N., Kouyama, T., Murakami, S.-Y., Nakamura, M., Ogohara, K., Sato, M., Sato, T.M., Suzuki, M., Taguchi, M., Takagi, S., Ueno, M., Watanabe, S., Yamada, M., Yamazaki, A., 2017. Large stationary gravity wave in the atmosphere of Venus. Nat. Geosci. 10 (2), 85–88. http://dx.doi.org/10.1038/ngeo2873.

Garate-Lopez, I., Lebonnois, S., 2018. Latitudinal variation of clouds' structure responsible for Venus' cold collar. Icarus 314, 1–11. http://dx.doi.org/10.1016/j.icarus.2018.05.011.

Gérard, J.C., Bougher, S.W., López-Valverde, M.A., Pätzold, M., Drossart, P., Piccioni, G., 2017. Aeronomy of the venus upper atmosphere. Space Sci. Rev. 212 (3–4), 1617–1683. http://dx.doi.org/10.1007/s11214-017-0422-0.

Gérard, J.-C., Saglam, A., Piccioni, G., Drossart, P., Montmessin, F., Bertaux, J.-L., 2009. Atomic oxygen distribution in the Venus mesosphere from observations of O_2 infrared airglow by VIRTIS-Venus express. Icarus 199 (2), 264–272. http://dx.doi.org/10.1016/j.icarus.2008.09.016.

Gérard, J.C., Soret, L., Piccioni, G., Drossart, P., 2014. Latitudinal structure of the Venus O_2 infrared airglow: A signature of small-scale dynamical processes in the upper atmosphere. Icarus 236, 92–103. http://dx.doi.org/10.1016/j.icarus.2014.03.028.

Gilli, G., Lebonnois, S., González-Galindo, F., López-Valverde, M.A., Stolzenbach, A., Lefèvre, F., Chaufray, J.Y., Lott, F., 2017. Thermal structure of the upper atmosphere of Venus simulated by a ground-to-thermosphere GCM. Icarus 281, 55–72. http://dx.doi.org/10.1016/j.icarus.2016.09.016.

Gilli, G., López-Valverde, M.A., Peralta, J., Bougher, S., Brecht, A., Drossart, P., Piccioni, G., 2015. Carbon monoxide and temperature in the upper atmosphere of Venus from VIRTIS/Venus Express non-LTE limb measurements. Icarus 248, 478–498. http://dx.doi.org/10.1016/j.icarus.2014.10.047.

Gilli, G., Navarro, T., Lebonnois, S., Quirino, D., Silva, V., Stolzenbach, A., Lefèvre, F., Schubert, G., 2021. Venus upper atmosphere revealed by a gcm: ii. model validation with temperature and density measurements. Icarus 114432. http://dx.doi.org/10.1016/j.icarus.2021.114432.

Gorinov, D.A., Khatuntsev, I.V., Zasova, L.V., Turin, A.V., Piccioni, G., 2018. Circulation of venusian atmosphere at 90-110 km based on apparent motions of the O_2 1.27 μm nightglow from VIRTIS-M (Venus Express) data. Geophys. Res. Lett. 45 (5), 2554–2562. http://dx.doi.org/10.1002/2017GL076380.

Haus, R., Kappel, D., Arnold, G., 2015. Radiative heating and cooling in the middle and lower atmosphere of Venus and responses to atmospheric and spectroscopic parameter variations. Planet. Space Sci. 117, 262–294. http://dx.doi.org/10.1016/j.pss.2015.06.024.

Hedin, A.E., Niemann, H.B., Kasprzak, W.T., Seiff, A., 1983. Global empirical model of the Venus thermosphere. J. Geophys. Res.: Space Phys. 88 (A1), 73–84. http://dx.doi.org/10.1029/JA088iA01p00073.

Heng, K., 2012. On the existence of shocks in irradiated exoplanetary atmospheres. Astrophys. J. Lett. 761 (1), L1. http://dx.doi.org/10.1088/2041-8205/761/1/L1, arXiv:1210.8243.

Hoshino, N., Fujiwara, H., Takagi, M., Kasaba, Y., 2013. Effects of gravity waves on the day-night difference of the general circulation in the Venusian lower thermosphere. J. Geophys. Res. (Planets) 118 (10), 2004–2015. http://dx.doi.org/10.1002/jgre.20154.

Hoshino, N., Fujiwara, H., Takagi, M., Takahashi, Y., Kasaba, Y., 2012. Characteristics of planetary-scale waves simulated by a new venusian mesosphere and thermosphere general circulation model. Icarus 217 (2), 818–830. http://dx.doi.org/10.1016/j.icarus.2011.06.039.

Hourdin, F., Musat, I., Bony, S., Braconnot, P., Codron, F., Dufresne, J.-L., Fairhead, L., Filiberti, M.-A., Friedlingstein, P., Grandpeix, J.-Y., Krinner, G., Levan, P., Li, Z.-X., Lott, F., 2006. The LMDZ4 general circulation model: climate performance and sensitivity to parametrized physics with emphasis on tropical convection. Clim. Dynam. 27 (7–8), 787–813. http://dx.doi.org/10.1007/s00382-006-0158-0.

Hueso, R., Sánchez-Lavega, A., Piccioni, G., Drossart, P., Gérard, J.C., Khatuntsev, I., Zasova, L., Migliorini, A., 2008. Morphology and dynamics of Venus oxygen airglow from Venus Express/Visible and Infrared Thermal Imaging Spectrometer observations. J. Geophys. Res. (Planets) 113, E00B02. http://dx.doi.org/10.1029/2008JE003081.

Imai, M., Kouyama, T., Takahashi, Y., Yamazaki, A., Watanabe, S., Yamada, M., Imamura, T., Satoh, T., Nakamura, M., Murakami, S.-y., et al., 2020. Planetary-scale variations in winds and UV brightness at the Venusian cloud top: Periodicity and temporal evolution. J. Geophys. Res. (Planets) 124 (10), 2635–2659. http://dx.doi.org/10.1029/2019JE006065.

Imai, M., Takahashi, Y., Watanabe, M., Kouyama, T., Watanabe, S., Gouda, S., Gouda, Y., 2016. Ground-based observation of the cyclic nature and temporal variability of planetary-scale UV features at the Venus cloud top level. Icarus 278, 204–214. http://dx.doi.org/10.1016/j.icarus.2016.06.011.

Imamura, T., Higuchi, T., Maejima, Y., Takagi, M., Sugimoto, N., Ikeda, K., Ando, H., 2014. Inverse insolation dependence of Venus' cloud-level convection. Icarus 228, 181–188. http://dx.doi.org/10.1016/j.icarus.2013.10.012.

Kane, S.R., Arney, G., Crisp, D., Domagal-Goldman, S., Glaze, L.S., Goldblatt, C., Grinspoon, D., Head, J.W., Lenardic, A., Unterborn, C., Way, M.J., Zahnle, K.J., 2019. Venus as a laboratory for exoplanetary science. J. Geophys. Res. (Planets) 124 (8), 2015–2028. http://dx.doi.org/10.1029/2019JE005939, arXiv:1908.02783.

Kashimura, H., Sugimoto, N., Takagi, M., Matsuda, Y., Ohfuchi, W., Enomoto, T., Nakajima, K., Ishiwatari, M., Sato, T.M., Hashimoto, G.L., Satoh, T., Takahashi, Y.O., Hayashi, Y.-Y., 2019. Planetary-scale streak structure reproduced in high-resolution simulations of the Venus atmosphere with a low-stability layer. Nature Commun. 10, 23. http://dx.doi.org/10.1038/s41467-018-07919-y.

Kouyama, T., Imamura, T., Nakamura, M., Satoh, T., Futaana, Y., 2015. Vertical propagation of planetary-scale waves in variable background winds in the upper cloud region of Venus. Icarus 248, 560–568. http://dx.doi.org/10.1016/j.icarus.2014.07.011.

Kouyama, T., Imamura, T., Taguchi, M., Fukuhara, T., Sato, T.M., Yamazaki, A., Futaguchi, M., Murakami, S., Hashimoto, G.L., Ueno, M., Iwagami, N., Takagi, S., Takagi, M., Ogohara, K., Kashimura, H., Horinouchi, T., Sato, N., Yamada, M., Yamamoto, Y., Ohtsuki, S., Sugiyama, K., Ando, H., Takamura, M., Yamada, T., Satoh, T., Nakamura, M., 2017. Topographical and local time dependence of large stationary gravity waves observed at the cloud top of venus. Geophys. Res. Lett. 44 (24), 12,098–12,105. http://dx.doi.org/10.1002/2017GL075792.

Krasnopolsky, V.A., 2011. Excitation of the oxygen nightglow on the terrestrial planets. Planet. Space Sci. 59 (8), 754–766. http://dx.doi.org/10.1016/j.pss.2011.02.015.

Krause, P., Sornig, M., Wischnewski, C., Kostiuk, T., Livengood, T.A., Herrmann, M., Sonnabend, G., Stangier, T., Wiegand, M., Pätzold, M., Mahieux, A., Vandaele, A.C., Piccialli, A., Montmessin, F., 2018. Long term evolution of temperature in the venus upper atmosphere at the evening and morning terminators. Icarus 299, 370–385. http://dx.doi.org/10.1016/j.icarus.2017.07.030.

Lafferty, W.J., Solodov, A.M., Lugez, C.L., Fraser, G.T., 1998. Rotational line strengths and self-pressure-broadening coefficients for the 1.27-μm, a 1 δ g–x 3 σ g-, v= 0–0 band of O_2. Appl. Opt. 37 (12), 2264–2270. http://dx.doi.org/10.1364/AO.37.002264.

Lebonnois, S., Covey, C., Grossman, A., Parish, H., Schubert, G., Walterscheid, R., Lauritzen, P., Jablonowski, C., 2012. Angular momentum budget in general circulation models of superrotating atmospheres: A critical diagnostic. J. Geophys. Res. (Planets) 117 (E12), E12004. http://dx.doi.org/10.1029/2012JE004223.

Lebonnois, S., Hourdin, F., Eymet, V., Crespin, A., Fournier, R., Forget, F., 2010. Superrotation of Venus' atmosphere analyzed with a full general circulation model. J. Geophys. Res. (Planets) 115 (E6), E06006. http://dx.doi.org/10.1029/2009JE003458.

Lebonnois, S., Sugimoto, N., Gilli, G., 2016. Wave analysis in the atmosphere of Venus below 100-km altitude, simulated by the LMD Venus GCM. Icarus 278, 38–51. http://dx.doi.org/10.1016/j.icarus.2016.06.004.

Lefèvre, M., Lebonnois, S., Spiga, A., 2018. Three-dimensional turbulence-resolving modeling of the venusian cloud layer and induced gravity waves: Inclusion of complete radiative transfer and wind shear. J. Geophys. Res. (Planets) 123 (10), 2773–2789. http://dx.doi.org/10.1029/2018JE005679.

Lefèvre, M., Spiga, A., Lebonnois, S., 2020. Mesoscale modeling of Venus' bow-shape waves. Icarus 335, 113376. http://dx.doi.org/10.1016/j.icarus.2019.07.010, arXiv:1902.07010.

Lellouch, E., Clancy, T., Crisp, D., Kliore, A.J., Titov, D., Bougher, S.W., 1997. Monitoring of mesospheric structure and dynamics. In: Bougher, S.W., Hunten, D.M., Phillips, R.J. (Eds.), Venus II: Geology, Geophysics, Atmosphere, and Solar Wind Environment. p. 295.

Liepmann, H.W., Roshko, A., 2001. Elements of Gas Dynamics. Courier Corporation.

Lott, F., Guez, L., Maury, P., 2012. A stochastic parameterization of non-orographic gravity waves: Formalism and impact on the equatorial stratosphere. Geophys. Res. Lett. 39 (6), L06807. http://dx.doi.org/10.1029/2012GL051001.

Lundin, R., Barabash, S., Futaana, Y., Sauvaud, J.A., Fedorov, A., Perez-de-Tejada, H., 2011. Ion flow and momentum transfer in the Venus plasma environment. Icarus 215 (2), 751–758. http://dx.doi.org/10.1016/j.icarus.2011.06.034.

Mahieux, A., Vandaele, A.C., Bougher, S.W., Drummond, R., Robert, S., Wilquet, V., Chamberlain, S., Piccialli, A., Montmessin, F., Tellmann, S., Pätzold, M., Häusler, B., Bertaux, J.L., 2015. Update of the venus density and temperature profiles at high altitude measured by SOIR on board Venus express. Planet. Space Sci. 113, 309–320. http://dx.doi.org/10.1016/j.pss.2015.02.002.

Marcq, E., Mills, F.P., Parkinson, C.D., Vandaele, A.C., 2018. Composition and chemistry of the neutral atmosphere of venus. Space Sci. Rev. 214 (1), 10. http://dx.doi.org/10.1007/s11214-017-0438-5.

Masunaga, K., Seki, K., Terada, N., Tsuchiya, F., Kimura, T., Yoshioka, K., Murakami, G., Yamazaki, A., Kagitani, M., Tao, C., Fedorov, A., Futaana, Y., Zhang, T.L., Shiota, D., Leblanc, F., Chaufray, J.Y., Yoshikawa, I., 2015. Periodic variations of oxygen EUV dayglow in the upper atmosphere of Venus: Hisaki/EXCEED observations. J. Geophys. Res. (Planets) 120 (12), 2037–2052. http://dx.doi.org/10.1002/2015JE004849.

Masunaga, K., Seki, K., Terada, N., Tsuchiya, F., Kimura, T., Yoshioka, K., Murakami, G., Yamazaki, A., Tao, C., Leblanc, F., Yoshikawa, I., 2017. Dawn-dusk difference of periodic oxygen EUV dayglow variations at Venus observed by Hisaki. Icarus 292, 102–110. http://dx.doi.org/10.1016/j.icarus.2016.12.027.

Mellor, G.L., Yamada, T., 1982. Development of a turbulence closure model for geophysical fluid problems. Rev. Geophys. Space Phys. 20, 851. http://dx.doi.org/10.1029/RG020i004p00851.

Nakagawa, H., Hoshino, N., Sornig, M., Kasaba, Y., Sonnabend, G., Stupar, D., Aoki, S., Murata, I., 2013. Comparison of general circulation model atmospheric wave simulations with wind observations of venusian mesosphere. Icarus 225 (1), 840–849. http://dx.doi.org/10.1016/j.icarus.2013.02.029.

Nakamura, M., Imamura, T., Ishii, N., Abe, T., Kawakatsu, Y., Hirose, C., Satoh, T., Suzuki, M., Ueno, M., Yamazaki, A., et al., 2016. AKATSUKI Returns to Venus. Earth Planets Space 68 (1), 1–10. http://dx.doi.org/10.1186/s40623-016-0457-6.

Nara, Y., Imamura, T., Masunaga, K., Lee, Y.Â.J., Terada, N., Yoshioka, K., Yamazaki, A., Seki, K., Yoshikawa, I., Yamada, M., Watanabe, S., 2020. Vertical coupling between the cloud-level atmosphere and the thermosphere of venus inferred from the simultaneous observations by Hisaki and Akatsuki. J. Geophys. Res. (Planets) 125 (3), e06192. http://dx.doi.org/10.1029/2019JE006192.

Nara, Y., Imamura, T., Murakami, S., Kouyama, T., Ogohara, K., Yamada, M., Takagi, M., Kashimura, H., Sato, N., 2019. Formation of the Y feature at the venusian cloud top by planetary-scale waves and the mean circulation: Analysis of venus express VMC images. J. Geophys. Res. (Planets) 124 (5), 1143–1156. http://dx.doi.org/10.1029/2018JE005779.

Navarro, T., Schubert, G., Lebonnois, S., 2018. Atmospheric mountain wave generation on Venus and its influence on the solid planet's rotation rate. Nat. Geosci. 11 (7), 487–491. http://dx.doi.org/10.1038/s41561-018-0157-x.

Ohtsuki, S., Iwagami, N., Sagawa, H., Ueno, M., Kasaba, Y., Imamura, T., Yanagisawa, K., Nishihara, E., 2008. Distributions of the Venus 1.27-μm O_2 airglow and rotational temperature. Planet. Sci. 56 (10), 1391–1398. http://dx.doi.org/10.1016/j.pss.2008.05.013.

Peralta, J., Hueso, R., Sánchez-Lavega, A., Lee, Y.J., Muñoz, A.G., Kouyama, T., Sagawa, H., Sato, T.M., Piccioni, G., Tellmann, S., Imamura, T., Satoh, T., 2017. Stationary waves and slowly moving features in the night upper clouds of Venus. Nat. Astron. 1, 0187. http://dx.doi.org/10.1038/s41550-017-0187, arXiv:1707.07796.

Peralta, J., Navarro, T., Vun, C.W., Sánchez-Lavega, A., McGouldrick, K., Horinouchi, T., Imamura, T., Hueso, R., Boyd, J.P., Schubert, G., Kouyama, T., Satoh, T., Iwagami, N., Young, E.F., Bullock, M.A., Machado, P., Lee, Y.J., Limaye, S.S., Nakamura, M., Tellmann, S., Wesley, A., Miles, P., 2020. A long-lived sharp disruption on the lower clouds of venus. Geophys. Res. Lett. 47 (11), e87221. http://dx.doi.org/10.1029/2020GL087221, arXiv:2005.13540.

Peralta, J., Sánchez-Lavega, A., López-Valverde, M.A., Luz, D., Machado, P., 2015. Venus's major cloud feature as an equatorially trapped wave distorted by the wind. Geophys. Res. Lett. 42 (3), 705–711. http://dx.doi.org/10.1002/2014GL062280.

Piccialli, A., Montmessin, F., Belyaev, D., Mahieux, A., Fedorova, A., Marcq, E., Bertaux, J.L., Tellmann, S., Vandaele, A.C., Korablev, O., 2015. Thermal structure of Venus nightside upper atmosphere measured by stellar occultations with SPICAV/Venus express. Planet. Space Sci. 113, 321–335. http://dx.doi.org/10.1016/j.pss.2014.12.009.

Piccialli, A., Moreno, R., Encrenaz, T., Fouchet, T., Lellouch, E., Widemann, T., 2017. Mapping the thermal structure and minor species of Venus mesosphere with ALMA submillimeter observations. Astron. Astrophys. 606, A53. http://dx.doi.org/10.1051/0004-6361/201730923.

Rauscher, E., Menou, K., 2010. Three-dimensional modeling of hot jupiter atmospheric flows. Astrophys. J. 714 (2), 1334–1342. http://dx.doi.org/10.1088/0004-637X/714/2/1334, arXiv:0907.2692.

Royer, E., Montmessin, F., Bertaux, J.-L., 2010. NO Emissions as observed by SPICAV during stellar occultations. Planet. Space Sci. 58 (10), 1314–1326. http://dx.doi.org/10.1016/j.pss.2010.05.015.

Schubert, G., 1983. General circulation and the dynamical state of the Venus atmosphere. In: Venus. pp. 681–765.

Schubert, G., Bougher, S.W., Covey, C.C., Del Genio, A.D., Grossman, A.S., Hollingsworth, J.L., Limaye, S.S., Young, R.E., 2007. Venus Atmosphere Dynamics: a Continuing Enigma. In: Washington DC American Geophysical Union Geophysical Monograph Series, vol. 176, pp. 101–120. http://dx.doi.org/10.1029/176GM07.

Schubert, G., Covey, C., del Genio, A., Elson, L.S., Keating, G., Seiff, A., Young, R.E., Apt, J., Counselman, C.C., Kliore, A.J., Limaye, S.S., Revercomb, H.E., Sromovsky, L.A., Suomi, V.E., Taylor, F., Woo, R., von Zahn, U., 1980. Structure and circulation of the Venus atmosphere. J. Geophys. Res.: Space Phys. 85, 8007–8025. http://dx.doi.org/10.1029/JA085iA13p08007.

Seiff, A., 1982. Dynamical implications of the observed thermal contrasts in Venus' upper atmosphere. Icarus 51 (3), 574–592. http://dx.doi.org/10.1016/0019-1035(82)90147-6.

Showman, A.P., Fortney, J.J., Lian, Y., Marley, M.S., Freedman, R.S., Knutson, H.A., Charbonneau, D., 2009. Atmospheric circulation of hot jupiters: Coupled radiative-dynamical general circulation model simulations of HD 189733b and HD 209458b. Agron. J. 699 (1), 564–584. http://dx.doi.org/10.1088/0004-637X/699/1/564, arXiv:0809.2089.

Soret, L., Gérard, J.-C., 2015. Is the $O_2(a^1\Delta_g)$ venus nightglow emission controlled by solar activity? Icarus 262, 170–172. http://dx.doi.org/10.1016/j.icarus.2015.08.030.

Soret, L., Gérard, J.C., Montmessin, F., Piccioni, G., Drossart, P., Bertaux, J.L., 2012. Atomic oxygen on the Venus nightside: Global distribution deduced from airglow mapping. Icarus 217 (2), 849–855. http://dx.doi.org/10.1016/j.icarus.2011.03.034.

Soret, L., Gérard, J.-C., Piccioni, G., Drossart, P., 2014. Time variations of $O_2(a^1\Delta)$ nightglow spots on the Venus nightside and dynamics of the upper mesosphere. Icarus 237, 306–314. http://dx.doi.org/10.1016/j.icarus.2014.03.034.

Sornig, M., Livengood, T., Sonnabend, G., Kroetz, P., Stupar, D., Kostiuk, T., Schieder, R., 2008. Venus upper atmosphere winds from ground-based heterodyne spectroscopy of CO_2 at 10μm wavelength. Planet. Space Sci. 56 (10), 1399–1406. http://dx.doi.org/10.1016/j.pss.2008.05.006.

Sornig, M., Livengood, T.A., Sonnabend, G., Stupar, D., Kroetz, P., 2012. Direct wind measurements from November 2007 in Venus' upper atmosphere using ground-based heterodyne spectroscopy of CO_2 at 10 μm wavelength. Icarus 217 (2), 863–874. http://dx.doi.org/10.1016/j.icarus.2011.03.019.

Sornig, M., Sonnabend, G., Stupar, D., Kroetz, P., Nakagawa, H., Mueller-Wodarg, I., 2013. Venus' upper atmospheric dynamical structure from ground-based observations shortly before and after Venus' inferior conjunction 2009. Icarus 225 (1), 828–839. http://dx.doi.org/10.1016/j.icarus.2012.12.005.

Stewart, A.I.F., Gerard, J.C., Rusch, D.W., Bougher, S.W., 1980. Morphology of the venus ultraviolet night airglow. J. Geophys. Res.: Space Phys. 85, 7861–7870. http://dx.doi.org/10.1029/JA085iA13p07861.

Stiepen, A., Gérard, J.C., Dumont, M., Cox, C., Bertaux, J.L., 2013. Venus nitric oxide nightglow mapping from SPICAV nadir observations. Icarus 226 (1), 428–436. http://dx.doi.org/10.1016/j.icarus.2013.05.031.

Stolzenbach, A., 2016. Étude de la photochimie de Vénus à l'aide d'un modèle de circulation générale. (Theses). UPMC - Université Paris 6 Pierre et Marie Curie, URL: https://hal.archives-ouvertes.fr/tel-01415771.

Sugimoto, N., Takagi, M., Matsuda, Y., 2014. Waves in a Venus general circulation model. Geophys. Res. Lett. 41 (21), 7461–7467. http://dx.doi.org/10.1002/2014GL061807.

Sugimoto, N., Yamazaki, A., Kouyama, T., Kashimura, H., Enomoto, T., Takagi, M., 2017. Development of an ensemble Kalman filter data assimilation system for the Venusian atmosphere. Sci. Rep. 7, 9321. http://dx.doi.org/10.1038/s41598-017-09461-1.

Svedhem, H., Titov, D.V., Taylor, F.W., Witasse, O., 2007. Venus as a more Earth-like planet. Nature 450 (7170), 629–632. http://dx.doi.org/10.1038/nature06432.

Takagi, M., Sugimoto, N., Ando, H., Matsuda, Y., 2018. Three-dimensional structures of thermal tides simulated by a Venus GCM. J. Geophys. Res. (Planets) 123 (2), 335–352. http://dx.doi.org/10.1002/2017JE005449.

Vallis, G.K., 2006. Atmospheric and Oceanic Fluid Dynamics. Cambridge University Press, http://dx.doi.org/10.1017/9781107588417.

Vandaele, A.C., De Mazière, M., Drummond, R., Mahieux, A., Neefs, E., Wilquet, V., Korablev, O., Fedorova, A., Belyaev, D., Montmessin, F., Bertaux, J.L., 2008. Composition of the Venus mesosphere measured by Solar Occultation at Infrared on board Venus Express. J. Geophys. Res. (Planets) 113 (13), E00B23. http://dx.doi.org/10.1029/2008JE003140.

Wang, C., Forget, F., Bertrand, T., Spiga, A., Millour, E., Navarro, T., 2018. Parameterization of rocket dust storms on mars in the LMD martian GCM: Modeling details and validation. J. Geophys. Res. (Planets).

Wang, P., Mitchell, J.L., 2014. Planetary ageostrophic instability leads to superrotation. Geophys. Res. Lett. 41 (12), 4118–4126. http://dx.doi.org/10.1002/2014GL060345.

Yamamoto, M., 2019. Equatorial kelvin-like waves on slowly rotating and/or small-sized spheres: Application to Venus and Titan. Icarus 322, 103–113. http://dx.doi.org/10.1016/j.icarus.2019.01.008.

Zalucha, A.M., Brecht, A.S., Rafkin, S., Bougher, S.W., Alexander, M.J., 2013. Incorporation of a gravity wave momentum deposition parameterization into the Venus Thermosphere General Circulation Model (VTGCM). J. Geophys. Res. (Planets) 118 (1), 147–160. http://dx.doi.org/10.1029/2012JE004168.

Zhang, S., Bougher, S.W., Alexander, M.J., 1996. The impact of gravity waves on the venus thermosphere and O_2 IR nightglow. J. Geophys. Res. (Planets) 101 (E10), 23195–23206. http://dx.doi.org/10.1029/96JE02035.

Zhu, Z., Stone, J.M., Rafikov, R.R., 2013. Low-mass planets in protoplanetary disks with net vertical magnetic fields: The planetary wake and gap opening. Astrophys. J. 768 (2), 143. http://dx.doi.org/10.1088/0004-637X/768/2/143, arXiv:1302.3239.